Available online at www.sciencedirect.com
ScienceDirect
Journal of Computational Physics 225 (2007) 237–262
JOURNAL OF COMPUTATIONAL PHYSICS
www.elsevier.com/locate/jcp

Magnetotelluric inversion via reverse time migration algorithm of seismic data

Taeyoung Ha [a,*], Changsoo Shin [b]

[a] Department of Mathematical Sciences, Seoul National University, San 56-1, Sillim-dong, Gwanak-gu, Seoul 151-747, Republic of Korea
[b] School of Civil, Urban and Geosystem Engineering, Seoul National University, San 56-1, Sillim-dong, Gwanak-gu, Seoul 151-742, Republic of Korea

Received 8 April 2006; received in revised form 26 November 2006; accepted 27 November 2006
Available online 11 January 2007

Abstract

We propose a new algorithm for two-dimensional magnetotelluric (MT) inversion. Our algorithm is an MT inversion based on the steepest descent method, borrowed from the backpropagation technique of seismic inversion or reverse time migration, introduced in the middle 1980s by Lailly and Tarantola. The steepest descent direction can be calculated efficiently by using the symmetry of numerical Green's function derived from a mixed finite element method proposed by Nédélec for Maxwell's equation, without calculating the Jacobian matrix explicitly. We construct three different objective functions by taking the logarithm of the complex apparent resistivity as introduced in the recent waveform inversion algorithm by Shin and Min. These objective functions can be naturally separated into amplitude inversion, phase inversion and simultaneous inversion. We demonstrate our algorithm by showing three inversion results for synthetic data.

Keywords: Magnetotelluric method; Logarithm of complex apparent resistivity; Backpropagation technique

1. Introduction

The magnetotelluric (MT) method is to delineate electric conductivity from telluric currents measured on the earth's surface. Since most inverse problems in geophysics are nonlinear, many people have tackled them using Newton-type methods such as Gauss–Newton methods and conjugate-gradient methods. Inversion using a Gauss–Newton method requires computation of both the Jacobian matrix and the Hessian matrix. To reduce the computational time and cost for calculating Jacobian matrix, Rodi [16] efficiently calculated the Jacobin matrix using reciprocity theorem. Reciprocity algorithm has been used also in seismic waveform inversion [20] and dc inversion [2]. Since the MT method is not a multiple-source problem, the use of reciprocity theorem in MT inversion is not as computationally economical as in seismic waveform inversion problem or the dc inversion problem. An improvement over the Gauss–Newton method is the Incomplete

* Corresponding author. Tel.: +82 2 880 6271; fax: +82 2 887 4694.
E-mail addresses: tyha@math.snu.ac.kr (T. Ha), css@model.snu.ac.kr (C. Shin).

0021-9991/$ - see front matter © 2006 Elsevier Inc. All rights reserved.
doi:10.1016/j.jcp.2006.11.024

Conjugate-Gradient method introduced by Mackie–Madden [8]. The Mackie–Madden algorithm uses a conjugate gradient iteration in which the matrix equation induced by the governing equation is solved incompletely. This algorithm requires one forward modeling per individual frequency at each iteration and the Jacobian matrix is calculated as sparse matrix–vector product without computing the Jacobian itself. Their algorithm was adapted by Zhang et al. [29] to 3-D resistivity inversion. Rodi and Mackie [17] proposed the nonlinear conjugate algorithm for 2-D MT inversion, which is similar to Mackie–Madden algorithm. Newman and Alumbaugh [13] extended the algorithm of Rodi and Mackie to 3-D MT inversion.

The main objective of our paper is to develop a new method for magnetotelluric inversion via a classical but simple steepest descent algorithm. In our new algorithm, we exploit the adjoint state of mixed finite element method for MT modeling in order to calculate the steepest descent direction without computing Jacobian matrix. As Pratt et al. [15] predicted in the frequency domain waveform inversion, the seismic waveform inversion based on backpropagation technique could be easily applied to dc inversion, MT inversion and EM inversion. The backpropagation technique is the efficient algorithm for waveform inversion of large-scale geological models [4,14,15,20]. Ha et al. [2] successfully implemented an adjoint state of mixed finite element technique for the Poisson equation and adumbrated the possibility of using the mixed finite element method for MT and EM inversion. The Ha et al. technique must define the electric field rather than apparent resistivity in order to exploit the adjoint state of the Poisson equation. By doing so, the dc inversion based on backpropagation technique has emerged as a new method for DC inverse problem.

In this paper on MT inversion, the objective function is based on the complex apparent resistivity, which is calculated by using the ratio of electric field to magnetic field [6]. The key point in this paper is to define the objective function using the logarithm of the complex apparent resistivity as introduced by Shin and Min [22] in seismic inversion. By taking the logarithm of the ratio of modeled field to measured field, Shin and Min separated the objective function into l_2 norm with amplitude-only or phase-only or both amplitude and phase. In this study, we follow their approach to define a new objective function for MT inversion, which leads naturally to the computation of the steepest descent direction, without computing the Jacobian matrix explicitly, by exploiting the symmetry of the Green's function of mixed finite element method derived for Maxwells' equation.

We begin by stating a governing equation for our MT inversion and briefly introduce the mixed finite element method for MT modeling. Then, we will discuss the theory of steepest descent method and backpropagation technique using the adjoint state of Maxwell's equations for our MT inversion. Finally, we demonstrate our algorithm by showing three inversion results via our algorithm.

2. The governing equation

2.1. Two-dimensional magnetotelluric modeling: TM mode

Time harmonic Maxwell's equations [11] are given as

$$(\sigma + \mathrm{i}\omega\epsilon)\mathbf{E} - \nabla \times \mathbf{H} = \mathbf{J}_s \tag{1a}$$

$$\mathrm{i}\omega\mu\mathbf{H} + \nabla \times \mathbf{E} = -\mathbf{M}_s, \tag{1b}$$

where $\mathbf{E}$ is the electric field and $\mathbf{H}$ the magnetic field; $\mathbf{J}_s$ is an electric current source and $\mathbf{M}_s$ is a magnetic moment source; ω, ϵ, μ, and σ denote an angular frequency, the electric permittivity, magnetic permeability and conductivity, respectively, which satisfy the following bounds for any complex vector ξ,

$$\begin{aligned} 0 < \varepsilon_*|\xi|^2 &\leqslant \left|\sum_{j,k} \varepsilon_{jk}\xi_j\overline{\xi_k}\right| \leqslant \varepsilon^*|\xi|^2, \\ 0 \leqslant \sigma_*|\xi|^2 &\leqslant \left|\sum_{j,k} \sigma_{jk}\xi_j\overline{\xi_k}\right| \leqslant \sigma^*|\xi|^2, \\ 0 < \mu_*|\xi|^2 &\leqslant \left|\sum_{j,k} \mu_{jk}\xi_j\overline{\xi_k}\right| \leqslant \mu^*|\xi|^2. \end{aligned} \tag{2}$$

For a 2-D magnetotelluric inversion, we limit the computational domain to the conductivity domain $z \geqslant 0$. Note that, as shown in Fig. 1, z is positive below the surface. In MT inversion, $\omega\varepsilon$ is close to $\frac{1}{2T}10^{-10}$, where T is the period of a micropulsation [6]. Neglecting $\omega\varepsilon$, the governing equation consisting of a two-dimensional vector function $\mathbf{E} = (E_x, E_z)$ and the scalar potential function $H = H_y$ is given by

$$\begin{aligned}
&\sigma E_x = -\frac{\partial H_y}{\partial z}, \quad \text{for } z > 0,\\
&\sigma E_z = \frac{\partial H_y}{\partial x}, \quad \text{for } z > 0, \qquad (3a)\\
&\frac{\partial E_x}{\partial z} - \frac{\partial E_z}{\partial x} = -\mathrm{i}\omega\mu H_y, \quad \text{for } z > 0,\\
&H_y = 1, \quad \text{for } z = 0. \qquad (3b)
\end{aligned}$$

By rearranging Eq. (3), we obtain the well-known TM-equation:

$$-\nabla \cdot \left(\frac{1}{\sigma}\nabla H_y\right) + \mathrm{i}\omega\mu H_y = 0. \qquad (4)$$

By introducing a two-dimensional curl for a vector function $\boldsymbol{\psi}$ and a scalar function ϕ, we can express $\nabla \times \boldsymbol{\psi}$ and $\nabla \times \phi$ as

$$\nabla \times \boldsymbol{\psi} = \frac{\partial \psi_x}{\partial z} - \frac{\partial \psi_z}{\partial x}, \quad \nabla \times \phi = \left(-\frac{\partial \phi}{\partial z}, \frac{\partial \phi}{\partial x}\right).$$

Using this notation, Eq. (3) can be rewritten as

$$\begin{aligned}
&\sigma\mathbf{E} - \nabla \times H = 0, \quad \text{for } z > 0, \qquad (5a)\\
&-\nabla \times \mathbf{E} - \mathrm{i}\omega\mu H = 0, \quad \text{for } z > 0, \qquad (5b)\\
&H = 1, \quad \text{for } z = 0. \qquad (5c)
\end{aligned}$$

In this study, we only consider the primary fields in our computation and neglect the secondary field for the moment. Let the primary field $E_{xp}(z)$ and $H_{yp}(z)$ be denoted as

$$\begin{aligned}
&E_x = A\mathrm{e}^{\mathrm{i}kz}, \qquad (6a)\\
&H_y = \frac{k}{\omega\mu}A\mathrm{e}^{\mathrm{i}kz}, \qquad (6b)
\end{aligned}$$

where $k^2 = \mathrm{i}\omega\mu\sigma_p$ is the square of the wavenumber, or k is related to the skin depth δ as follows:

$$k = (\mathrm{i}\omega\mu\sigma_p)^{1/2} = \frac{1+\mathrm{i}}{\delta}, \qquad (7)$$

where $\delta = (2/\omega\mu\sigma_p)^{1/2}$, and the electric conductivity $\sigma_p = \sigma_p(z)$ is a conductivity on horizontally layered earth with no inhomogeneity and is only dependent on the depth z [5,6,10].

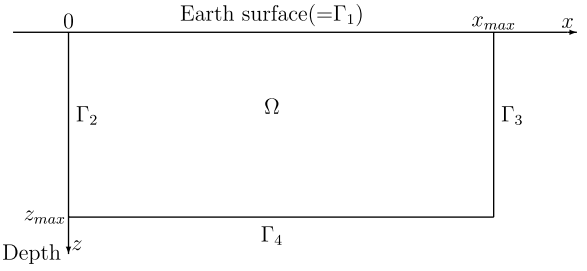

Fig. 1. Domain of resistivity exploration experiment. Ω is the computational domain. $z = 0$ is ground surface and z increases downwards. The boundary of the domain Ω is denoted by $\Gamma = \partial\Omega$, which is composed of the union of four parts, Γ_i, $i = 1, \ldots, 4$. Here, $\Gamma_1 = \{(x,z)|z = 0\}$, $\Gamma_2 = \{(x,z)|x = 0\}$, $\Gamma_3 = \{(x,z)|x = x_{\max}\}$ and $\Gamma_4 = \{(x,z)|z = z_{\max}\}$.

Here and in what follows, we define the scattered (secondary) electric vector field and magnetic scalar potential, $\mathbf{E}_s$ and H_s, respectively, and can express them as

$$\mathbf{E}_s = (E_x - E_{xp}, E_z),$$
$$H_s = H - H_{xp}.$$

Then, Eq. (5) becomes

$$\sigma \mathbf{E}_s - \nabla \times H_s = -\mathbf{g}, \quad \text{for } z > 0, \tag{8a}$$
$$-\nabla \times \mathbf{E}_s - \mathrm{i}\omega\mu H_s = 0, \quad \text{for } z > 0, \tag{8b}$$
$$H_s = 0, \quad \text{for } z = 0, \tag{8c}$$

where $\mathbf{g} = (\sigma - \sigma_p)(E_{xp}, 0)^{\mathrm{T}}$.

2.2. Boundary condition

We restrict the computational domain for Eq. (5) to two-dimensional bounded and conductive domain $\Omega = [0, x_{\max}] \times [0, z_{\max}]$ (see Fig. 1). The uppermost layer of Ω represents the interface separating the air and the conducting domain, as shown in Fig. 1. The computational domain is reduced to an isolated rectangular block with suitable boundary conditions. Then, we can divide the boundary of the computational domain Ω into four parts expressed as follows: $\Gamma_1 = \{(x,z)|0 < x < x_{\max}, z = 0\}$, $\Gamma_2 = \{(x,z)|0 < z < z_{\max}, x = 0\}$, $\Gamma_3 = \{(x,z)|0 < z < z_{\max}, x = x_{\max}\}$ and $\Gamma_4 = \{(x,z)|0 < x < x_{\max}, z = z_{\max}\}$. We apply following the boundary condition on Γ_1, Γ_2 and Γ_3:

$$H_s = 0, \quad \text{on } \Gamma_1, \tag{9a}$$
$$\frac{\partial H_s}{\partial x} = \mathbf{E}_s \cdot \boldsymbol{\tau} = 0, \quad \text{on } \Gamma_2 \quad \text{and} \quad \Gamma_3, \tag{9b}$$

where $\boldsymbol{\tau}$ is counterclockwise tangential vector [27]. In order to minimize the effect caused by the artificial boundaries, we impose the absorbing boundary condition introduced by Sheen [19]:

$$(1 - \mathrm{i})a\mathbf{E}_s \cdot \boldsymbol{\tau} + H_s = 0, \quad \text{on } \Gamma_4, \tag{10}$$

where $a = (\sigma/2\mu\omega)^{1/2}$ and $\boldsymbol{\tau}$ is the unit tangent vector to $\partial\Omega$.

2.3. Mixed finite element method

Numerical algorithms for MT modeling have been proposed by many geophysicists and applied mathematician over several decades [10,18,25,26,30]. Wannamaker et al. [25] used a finite element method to solve the two-dimensional scattering problem by using the standard formulation of Maxwell's equations. The MOM method for the forward calculation by finite element method was described in Rodi [16]. The MOM method is more useful in TM mode than TE mode. Mackie et al. [9] presented a finite difference procedure for three-dimensional magnetotelluric modeling. Recently, Santos et al. [18,30] and Ha et al. [3] proposed the parallel algorithm using domain decomposition method. In our numerical implementation, we adapted $\mathbf{H}(\mathbf{curl};\Omega)$-conforming finite element for Maxwell's equation suggested by Nédélec [12]. For a detailed numerical implementation, we refer the reader to deal.II of IWR [1].

The matrix equation for mixed problem in Eqs. (8)–(10) is given by

$$\mathbf{Ae} - \mathbf{Bh} + \mathbf{Ce} = \mathbf{s}, \tag{11a}$$
$$-\mathbf{B}^{\mathrm{T}}\mathbf{e} - \mathbf{Dh} = \mathbf{0}, \tag{11b}$$

where $\mathbf{A}$ and $\mathbf{D}$ are mass matrices, $\mathbf{B}$ is a stiffness matrix and $\mathbf{C}$ is a matrix obtained from the given boundary conditions. Note that $\mathbf{C}$ and $\mathbf{D}$ are diagonal matrices. $\mathbf{e}$ and $\mathbf{h}$ are the finite element solutions for electric field vector and magnetic scalar potential, respectively, and $\mathbf{s}$ is the source vector. Fig. 2 displays the nodes used for

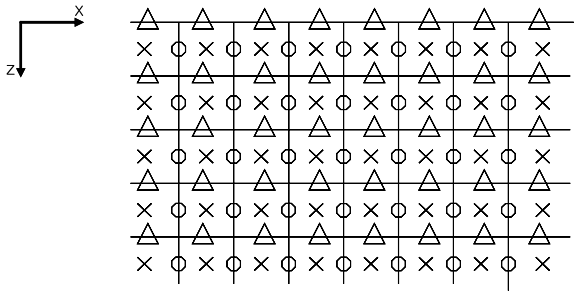

Fig. 2. Two-dimensional mesh in the computational domain. ○ represents the nodes for E_x, △ represents the nodes for E_z, and × represents the nodes for H_y.

computation of electric vector field and magnetic scalar potential. The magnetic potential is computed at the center of a element, whereas the electric field vector is computed at the average point of nodes of horizontally and vertically located adjacent nodes. By arranging Eq. (11), we have

$$\mathbf{K}\mathbf{u} = \mathbf{r}, \tag{12}$$

where

$$\mathbf{K} = \begin{pmatrix} \mathbf{A}+\mathbf{C} & -\mathbf{B} \\ -\mathbf{B}^{\mathrm{T}} & -\mathbf{D} \end{pmatrix}, \quad \mathbf{u} = \begin{pmatrix} \mathbf{e} \\ \mathbf{h} \end{pmatrix}, \quad \mathbf{r} = \begin{pmatrix} \mathbf{s} \\ \mathbf{0} \end{pmatrix}.$$

Since the governing equation is self-adjoint, we note that the matrix $\mathbf{K}$ is symmetric, which guarantees source and receiver reciprocity. Furthermore, we know that the matrices $\mathbf{A}$, $\mathbf{C}$, electric vector field $\mathbf{e}$, magnetic scalar potential $\mathbf{h}$ and source vector $\mathbf{r}$ are functions dependent on resistivity of the computational domain, which enables us to take derivative of them with respect to model parameter (resistivity).

3. Inverse theory

3.1. Mitfit functional

In the frequency domain, the transverse MT response represents the ratio of electric field to magnetic field. Following [17], we can define the complex apparent resistivity as follows:

$$\rho_{xy}^{c} = \frac{\mathrm{i}}{\omega\mu}\left(\frac{E_x}{H_y}\right)^2. \tag{13}$$

From Eq. (13), we define the amplitude and phase of apparent resistivity ρ_{xy}^{c}:

$$\rho_{xy} = \left|\rho_{xy}^{c}\right|, \quad \phi_{xy} = \mathbf{Arg}(\rho_{xy}^{c}).$$

Following Shin and Min's approach [22], we define the objective function Ψ as the l_2 norm of the logarithm amplitude ratio and phase difference as

$$\Psi(\mathbf{p}) = \frac{1}{2}\sum_{j_\omega=1}^{N_\omega}\sum_{j_r=1}^{N_r}\left[\left(\ln\frac{\rho_{xy}^{j_r}}{\rho_{xy}^{d,j_r}}\right)^2 + \left(\phi_{xy}^{j_r} - \phi_{xy}^{d,j_r}\right)^2\right], \tag{14}$$

where N_ω and N_r are the numbers of selected frequencies and receiver positions and $\mathbf{p} = (p_1, \ldots, p_J)$ is the model parameter vector. $\rho_{xy}^{j_r}$ and $\phi_{xy}^{j_r}$ are the amplitude and phase of the complex apparent resistivity computed for the current model and ρ_{xy}^{d,j_r} and ϕ_{xy}^{d,j_r} are the amplitude and phase of the complex apparent resistivity measured in the field. Note that we can separate the objective function expressed in Eq. (14) into two types. We can construct the objective function that is expressed as the amplitude ratio by neglecting the phase term in Eq. (14). Similarly, by omitting the amplitude ratio, we can build the objective function that consists of the phase difference only.

3.2. Steepest descent method using backpropagation technique

In the classical optimization technique, we iteratively update the model parameter vector **p** using the following relationship by computing the steepest descent direction of the given objective function with respect to model parameter:

$$p_k^{l+1} = p_k^l - \alpha^l \nabla_{p_k} \Psi(\mathbf{p}), \quad k = 1, \ldots, J \tag{15}$$

where l is the iteration number, α^l is the arbitrarily chosen step length and $\partial\Psi^l/\partial\rho^k$ is the direction normal to the contours of the constant objective function.

In order to implement the steepest descent direction, we need to compute the derivative of the objective function with respect to the model parameter vector **p**. Taking derivative of the objective function given by Eq. (14) yields

$$\begin{aligned}\nabla_{p_k}\boldsymbol{\Psi} &= \sum_{j_\omega=1}^{N_\omega}\sum_{j_r=1}^{N_r}\left[\left(\ln\frac{\rho_{xy}^{j_r}}{\rho_{xy}^{d,j_r}}\right)\frac{\partial}{\partial p_k}\left(\ln\frac{\rho_{xy}^{j_r}}{\rho_{xy}^{d,j_r}}\right)+\left(\phi_{xy}^{j_r}-\phi_{xy}^{d,j_r}\right)\frac{\partial\phi_{xy}^{j_r}}{\partial p_k}\right],\\ &= 2\sum_{j_\omega=1}^{N_\omega}\sum_{j_r=1}^{N_r}\left[\left(\ln\frac{\rho_{xy}^{j_r}}{\rho_{xy}^{d,j_r}}\right)\left(\frac{1}{e_x^{j_r}}\frac{\partial e_x^{j_r}}{\partial p_k}-\frac{1}{h_y^{j_r}}\frac{\partial h_y^{j_r}}{\partial p_k^{j_r}}\right)+\left(\phi_{xy}^{j_r}-\phi_{xy}^{d,j_r}\right)\left(\frac{\partial\theta_E^{j_r}}{\partial p_k}-\frac{\partial\theta_H^{j_r}}{\partial p_k}\right)\right],\end{aligned} \tag{16}$$

where $e_x^{j_r} = |E_x^{j_r}|$, $h_y^{j_r} = |H_y^{j_r}|$ and $\theta_E^{j_r} = \mathbf{Arg}(E_x^{j_r})$, $\theta_H^{j_r} = \mathbf{Arg}(H_y^{j_r})$. We can easily identify the following equations (see Appendix A):

$$\mathbf{Re}\left(\frac{1}{E_x}\frac{\partial E_x}{\partial p_k}\right)=\frac{1}{e_x}\frac{\partial e_x}{\partial p_k},\quad \mathbf{Im}\left(\frac{1}{E_x}\frac{\partial E_x}{\partial p_k}\right)=\frac{\partial\theta_E}{\partial p_k}, \tag{17a}$$

$$\mathbf{Re}\left(\frac{1}{E_z}\frac{\partial E_z}{\partial p_k}\right)=\frac{1}{e_z}\frac{\partial e_z}{\partial p_k},\quad \mathbf{Im}\left(\frac{1}{E_z}\frac{\partial E_z}{\partial p_k}\right)=\frac{\partial\theta_E}{\partial p_k}, \tag{17b}$$

$$\mathbf{Re}\left(\frac{1}{H_y}\frac{\partial H_y}{\partial p_k}\right)=\frac{1}{h_y}\frac{\partial h_y}{\partial p_k},\quad \mathbf{Im}\left(\frac{1}{H_y}\frac{\partial H_y}{\partial p_k}\right)=\frac{\partial\theta_H}{\partial p_k}. \tag{17c}$$

Substituting Eq. (17) into Eq. (16) yields Eq. (18)

$$\begin{aligned}\nabla_{p_k}\boldsymbol{\Psi} &= 2\sum_{j_\omega=1}^{N_\omega}\sum_{j_r=1}^{N_r}\left[\mathbf{Re}\left(r_{xy}^{j_r}\right)\mathbf{Re}\left(\frac{1}{E_x^{j_r}}\frac{\partial E_x^{j_r}}{\partial p_k}-\frac{1}{H_y^{j_r}}\frac{\partial H_y^{j_r}}{\partial p_k}\right)+\mathbf{Im}\left(r_{xy}^{j_r}\right)\mathbf{Im}\left(\frac{1}{E_x^{j_r}}\frac{\partial E_x^{j_r}}{\partial p_k}-\frac{1}{H_y^{j_r}}\frac{\partial H_y^{j_r}}{\partial p_k}\right)\right]\\ &= 2\sum_{j_\omega=1}^{N_\omega}\sum_{j_r=1}^{N_r}\mathbf{Re}\left[\left(\frac{1}{E_x^{j_r}}\frac{\partial E_x^{j_r}}{\partial p_k}-\frac{1}{H_y^{j_r}}\frac{\partial H_y^{j_r}}{\partial p_k}\right)\overline{\left(r_{xy}^{j_r}\right)}\right]=2\int_{-\infty}^{\infty}\sum_{j_r=1}^{N_r}\mathbf{Re}\left[\frac{\partial E_x^{j_r}}{\partial p_k}\frac{\partial H_y^{j_r}}{\partial p_k}\right]\begin{bmatrix}\frac{1}{E_x^{j_r}}\overline{\left(r_{xy}^{j_r}\right)}\\ -\frac{1}{H_y^{j_r}}\overline{\left(r_{xy}^{j_r}\right)}\end{bmatrix},\end{aligned} \tag{18}$$

where $r_{xy}^{j_r} = \ln\frac{E_x^{j_r}}{H_y^{j_r}} - \ln\frac{E_x^{d,j_r}}{H_y^{d,j_r}} = \ln\rho_{xy}^{c,j_r} - \ln\rho_{xy}^{c,d,j_r}$.

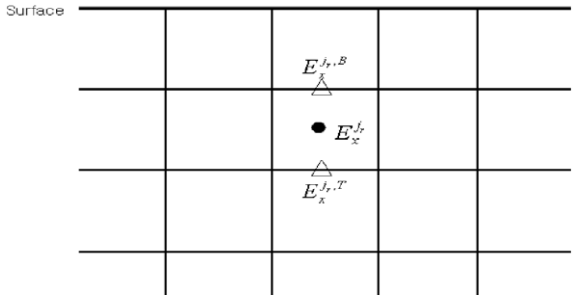

Fig. 3. Calculation of $E_x^{j_r}$ by interpolation between $E_x^{j_r,T}$ and $E_x^{j_r,B}$ at the j_rth measured points.

The apparent resistivities are calculated in the vicinity of the surface. In our numerical computational mesh shown in Fig. 3, we calculate the apparent resistivity at the center of an element and calculate E_x by taking its average at two adjacent nodes. We can express E_x as

$$E_x^{j_r} = \frac{1}{2}\left(E_x^{j_r,\mathrm{B}} + E_x^{j_r,\mathrm{T}}\right).$$

For convenience and to avoid confusion, we call $E_x^{j_r,\mathrm{B}}$ the B-node electric vector field and $E_x^{j_r,\mathrm{T}}$ the T-node electric vector field, respectively. By using these notations, we can express Eq. (18) as

$$\begin{aligned}\nabla_{p_k}\boldsymbol{\Psi} &= 2\sum_{j_\omega=1}^{N_\omega}\sum_{j_r=1}^{N_r}\mathbf{Re}\left[\frac{1}{2}\left(\frac{\partial E_x^{j_r,B}}{\partial p_k}+\frac{\partial E_x^{j_r,T}}{\partial p_k}\right)\frac{\partial H_y^{j_r}}{\partial p_k}\right]\begin{bmatrix}\frac{1}{E_x^{j_r}}\overline{\left(r_{xy}^{j_r}\right)}\\ -\frac{1}{H_y^{j_r}}\overline{\left(r_{xy}^{j_r}\right)}\end{bmatrix}\\ &= \mathbf{Re}\sum_{j_\omega=1}^{N_\omega}\sum_{j_r=1}^{N_r}\left(\begin{bmatrix}\frac{\partial E_x^{j_r,B}}{\partial p_k} & \frac{\partial H_y^{j_r}}{\partial p_k}\end{bmatrix}\begin{bmatrix}\frac{1}{E_x^{j_r}}\overline{\left(r_{xy}^{j_r}\right)}\\ -\frac{1}{H_y^{j_r}}\overline{\left(r_{xy}^{j_r}\right)}\end{bmatrix}+\begin{bmatrix}\frac{\partial E_x^{j_r,T}}{\partial p_k} & \frac{\partial H_y^{j_r}}{\partial p_k}\end{bmatrix}\begin{bmatrix}\frac{1}{E_x^{j_r}}\overline{\left(r_{xy}^{j_r}\right)}\\ -\frac{1}{H_y^{j_r}}\overline{\left(r_{xy}^{j_r}\right)}\end{bmatrix}\right).\end{aligned} \tag{19}$$

In Eq. (19), we regard $E_{x,\mathrm{s}}$ as the x component of $\mathbf{E}_\mathrm{s}$. Since $E_x = E_{xp} + E_{x,\mathrm{s}}$ and $H = H_{xp} + H_\mathrm{s}$, we know that

$$\frac{\partial E_x^{j_r,\mathrm{B}}}{\partial p_k} = \frac{\partial E_{x,s}^{j_r,\mathrm{B}}}{\partial p_k}, \quad \frac{\partial E_x^{j_r,\mathrm{T}}}{\partial p_k} = \frac{\partial E_{x,s}^{j_r,\mathrm{T}}}{\partial p_k} \quad \text{and} \quad \frac{\partial H^{j_r}}{\partial p_k} = \frac{\partial H_s^{j_r}}{\partial p_k}.$$

Using the above relations, Eq. (19) can be rewritten as Eq. (20)

$$\nabla_{p_k}\boldsymbol{\Psi} = \mathbf{Re}\sum_{j_\omega=1}^{N_\omega}\left[\frac{\partial E_{x,\mathrm{s}}^{1,\mathrm{B}}}{\partial p_k}\cdots\frac{\partial E_{x,\mathrm{s}}^{N_r,\mathrm{B}}}{\partial p_k}\frac{\partial H_{y,\mathrm{s}}^{1}}{\partial p_k}\cdots\frac{\partial H_{y,\mathrm{s}}^{N_r}}{\partial p_k}\right]\begin{bmatrix}\frac{1}{E_x^1}\overline{\left(r_{xy}^1\right)}\\ \vdots\\ \frac{1}{E_x^{N_r}}\overline{\left(r_{xy}^{N_r}\right)}\\ -\frac{1}{H_y^1}\overline{\left(r_{xy}^1\right)}\\ \vdots\\ -\frac{1}{H_y^{N_r}}\overline{\left(r_{xy}^{N_r}\right)}\end{bmatrix}+\left[\frac{\partial E_{x,\mathrm{s}}^{1,\mathrm{T}}}{\partial p_k}\cdots\frac{\partial E_{x,\mathrm{s}}^{N_r,\mathrm{T}}}{\partial p_k}\frac{\partial H_{y,\mathrm{s}}^{1}}{\partial p_k}\cdots\frac{\partial H_{y,\mathrm{s}}^{N_r}}{\partial p_k}\right]\begin{bmatrix}\frac{1}{E_x^1}\overline{\left(r_{xy}^1\right)}\\ \vdots\\ \frac{1}{E_x^{N_r}}\overline{\left(r_{xy}^{N_r}\right)}\\ -\frac{1}{H_y^1}\overline{\left(r_{xy}^1\right)}\\ \vdots\\ -\frac{1}{H_y^{N_r}}\overline{\left(r_{xy}^{N_r}\right)}\end{bmatrix}. \tag{20}$$

Let

$$\mathbf{u} = \left[E_{x,\mathrm{s}}^1\cdots E_{x,\mathrm{s}}^{N_r}\cdots E_{x,\mathrm{s}}^{J_{E_x}}E_{z,\mathrm{s}}^1\cdots E_{z,\mathrm{s}}^{N_r}\cdots E_{z,\mathrm{s}}^{J_{E_z}}H_{y,\mathrm{s}}^1\cdots H_{y,\mathrm{s}}^{N_r}\cdots H_{y,\mathrm{s}}^{J_{H_y}}\right]^\mathrm{T},$$

where J_{E_x}, J_{E_z} and J_{H_y} are the numbers of unknown parameters for E_x, E_z and H_y, respectively. Then, we can rewrite Eq. (20) as

$$\nabla_{p_k}\boldsymbol{\Psi} = \mathbf{Re}\sum_{j_\omega=1}^{N_\omega}\left(\frac{\partial \mathbf{u}^\mathrm{T}}{\partial p_k}\tilde{\mathbf{r}}_\mathrm{B} + \frac{\partial \mathbf{u}^\mathrm{T}}{\partial p_k}\tilde{\mathbf{r}}_\mathrm{T}\right). \tag{21}$$

Here, $\tilde{\mathbf{r}}_\mathrm{B}$ and $\tilde{\mathbf{r}}_\mathrm{T}$ are $(J_{E_x}+J_{E_z}+J_{H_y})\times 1$ vectors, which are composed of $\frac{1}{E_x^j}\overline{(r_{xy}^j)}$, $j=1,\ldots,J_{E_x}$, and $\frac{1}{H_y^k}\overline{(r_{xy}^k)}$, $k=1,\ldots,J_{H_y}$. By using augmenting zeroes in entries except those corresponding to receivers, we can express $\tilde{\mathbf{r}}_\mathrm{B}$ and $\tilde{\mathbf{r}}_\mathrm{T}$ as

$$\left[\frac{1}{E_x^1}\overline{\left(r_{xy}^1\right)}\cdots\frac{1}{E_x^{N_r}}\overline{\left(r_{xy}^{N_r}\right)}0\cdots 0\frac{-1}{H_y^1}\overline{\left(r_{xy}^1\right)}\cdots\frac{-1}{H_y^{N_r}}\overline{\left(r_{xy}^{N_r}\right)}0\cdots 0\right]^\mathrm{T}, \tag{22}$$

where entries of $\tilde{\mathbf{r}}_\mathrm{B}$ correspond to T-node of receiver position from 1 to N_r with augmented receiver locations and entries of $\tilde{\mathbf{r}}_\mathrm{T}$ correspond to B-node of receiver position from 1 to N_r with augmented receiver locations.

(For T- and B-node, see Fig. 3). By taking derivative of Eq. (12) with respect to the kth model parameter as Rodi [16] and Pratt et al. [15] did, we can express the partial derivatives of the electric vector field and magnetic scalar potential as

$$\frac{\partial \mathbf{K}}{\partial p_k}\mathbf{u} + \mathbf{K}\frac{\partial \mathbf{u}}{\partial p_k} = \frac{\partial \mathbf{r}}{\partial p_k},$$
$$\frac{\partial \mathbf{u}}{\partial p_k} = \mathbf{K}^{-1}\left[-\frac{\partial \mathbf{K}}{\partial p_k}\mathbf{u} + \frac{\partial \mathbf{r}}{\partial p_k}\right]. \tag{23}$$

Let $\mathbf{f}^{*,k}$ be $-\frac{\partial \mathbf{K}}{\partial p_k}\mathbf{u} + \frac{\partial \mathbf{r}}{\partial p_k}$ and call it the virtual source vector required to compute the partial derivatives. Since $\frac{\partial \mathbf{K}}{\partial p_k}$ is expressed by an elemental matrix consisting of 4×4 nonzero elements and $\frac{\partial \mathbf{r}}{\partial p_k}$ has numerical supports at the four elements in the 4×1 column vector, the computation of $\mathbf{f}^{*,k}$ is a trivial task. By exploiting the symmetry of matrix $\mathbf{K}$ (adjoint state of mixed finite element method for the governing equation in this paper) and following Ha et al. [2], we can efficiently compute the steepest descent direction without computing the partial derivatives explicitly. With virtual source vector, we express the steepest descent direction as

$$\nabla_{p_k}\Psi = \mathbf{Re}\sum_{j_\omega=1}^{N_\omega}\left([\mathbf{f}^{*,k}]^{\mathrm{T}}(\mathbf{K}^{-1}\tilde{\mathbf{r}}_{\mathrm{B}}) + [\mathbf{f}^{*,k}]^{\mathrm{T}}(\mathbf{K}^{-1}\tilde{\mathbf{r}}_{\mathrm{T}})\right), \tag{24}$$

where $(\mathbf{K}^{-1})^{\mathrm{T}} = \mathbf{K}^{-1}$. Note that Eq. (24) is basically identical to the equation for reverse time migration of seismic data of Shin and Min [22] and for dc inversion by Ha et al. [2].

We have three steps for computing the steepest descent direction. First, we forward model data, compute the virtual source vector for each parameter and save it into core memory. Next, we compute the residual vector that is defined in Eq. (22) and forward model again. In exploration seismology, geophysicists call this procedure backpropagation of residuals and use it to generate the backpropagated field $\mathbf{K}^{-1}(\tilde{\mathbf{r}}_{\mathrm{B}} + \tilde{\mathbf{r}}_{\mathrm{T}})$. Finally, we compute the steepest descent direction by calculating the dot product of the virtual source and the backpropagated fields.

By substituting Eq. (24) into Eq. (15) and using the Levenberg–Marquardt method [7] or by introducing a damping term to regularize the steepest descent method, the steepest descent method for MT inversion can be rewritten as

$$p_k^{l+1} = p_k^l - \alpha^l \mathbf{Re}\sum_{j_\omega=1}^{N_\omega}\left[\mathrm{diag}(\mathbf{H}_a + \lambda\mathbf{I})^{-1}\right]_k [\mathbf{f}^{*,k}]^{\mathrm{T}}\left(\mathbf{K}^{-1}[\tilde{\mathbf{r}}_{\mathrm{B}} + \tilde{\mathbf{r}}_{\mathrm{T}}]\right), \quad k = 1,\ldots,M \tag{25}$$

where $\mathbf{I}$ is the identity matrix, λ is the damping factor, and $\mathbf{H}_a$ is the Hessian, which can be approximated by $\mathbf{H}_a \approx \mathrm{diag}(\mathbf{J}^{\mathrm{T}}\mathbf{J})$ [2,21]. In our algorithm, we replace the diagonal of the Hessian by a pseudo Hessian proposed by Shin et al. [20].

3.3. Advantage of MT inversion over the conventional Gauss–Newton method

In experiments of seismic, DC and EM exploration, we usually have multiple sources, ranging from few hundreds to hundreds of thousands. For inversion of these multiple source geophysical problems via the Gauss–Newton method, once we factor the resulting matrix generated from the finite element method or the finite difference method for corresponding equations, we must perform m backward and forward substitutions for efficient calculation of the Jacobian matrix and Hessian matrix, by invoking reciprocity theorem [22,2] (m is the number of source and receiver points that does not overlap for every source experiment). However, in our MT inversion,we need two backward and forward substitutions at each iteration in order to calculate the steepest descent direction of our given objective function. One of these is to calculate a complex apparent resistivity in forward modeling stage Eq. (12). The other is to backpropagate the residual vector defined in Eq. (14) in order to compute the backpropgated field. Hence, our backpropagation technique is better suited to MT inversion than any other geophysical problems such as dc, EM and seismic inverse problems.

4. Numerical experiment

Many geophysical investigations have suffered the lack of resolution with depth for MT inversion [23,28,8,17]. Our method also has difficulties to improve the depth resolution. In order to verify our inversion algorithm for synthetic data, we choose three geological models. One is a conductive body embedded in a homogeneous half space. Second is a model that have two conductive bodies layered in a homogeneous half space. Third is a model that more complex conductive bodies embedded in half space. For these three synthetic models, we compare the results of an optimization algorithm given by the objective function corresponding to amplitude-only or phase-only or both amplitude and phase, respectively.

Furthermore, we test two kind of parameterization by subdividing a given model into different sized cells. One is to parameterize the model cell by cell. The other is block parameterization. In case of block parameterization, the partial derivatives of apparent resistivity with respect to the resistivity block $\boldsymbol{\rho}_{\mathbf{B}}$ can be obtained by using

$$\frac{\partial \mathbf{E}_a}{\partial \boldsymbol{\rho}_{\mathbf{B}}} = \sum_{(i,j)\in \mathbf{B}} \frac{\partial \mathbf{E}_a}{\partial \rho(i,j)}.$$

For stop criterion, the RMS error $r(l)$ for iteration number l can be defined as

$$r(l) = \sqrt{\frac{\Psi^l(\boldsymbol{\rho})}{N}}n,$$

where N is the product of the numbers of receiver position and frequency. We terminate the iteration when $(r(l) - r(l+1))/r(1)$ is less than 10^{-5} for both cell parameterization and block parameterization. To prevent the oscillation of RMS error during iteration, we use a large damping factor and a small step length. Therefore we have slow convergence. Therefore, we experimented with the inversion of synthetic data by both cell and block parameterization.

In MT inversion, there are two choices in parameterizing the model parameter. One is to select the resistivity as model parameter, the other is to use the conductivity as model parameter. However, taking the logarithm of resistivity or conductivity leads to the same form of equation [24,2], and vice versa. In this paper, we choose our unknown as the resistivity ρ as our unknown.

In our numerical experiments, we used the frequency range from 0.01 to 100 Hz. This takes into account the skin effect. Different depths of penetration occur for different frequencies. This allows one to detect the variation of resistivity with depth. The proposed algorithm was implemented on the serial SMP machine equipped with Xeon 3.0 GHz. The CPU times needed for one iteration for Model I and Model II are about 45 s, and the CPU time needed for one iteration for Model III is about 20 s.

4.1. Model I: a rectangular block embedded in a homogeneous half space

The sizes of the surrounding homogeneous space and the conductive block are 40 km × 20 km and 8 km × 6 km, respectively. The resistivities of the background half space and the conductive body are

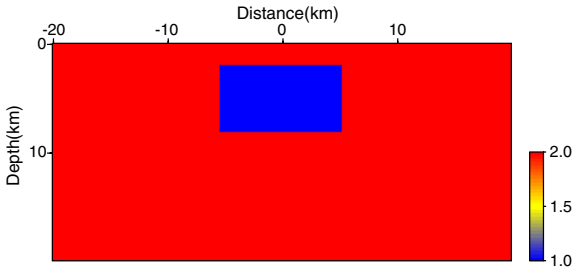

Fig. 4. 2-D true model used for resistivity inversion where the conductive block is located starting at 2 km depth from the earth surface. Resistivity scale has units $\log_{10}$ Ω-m.

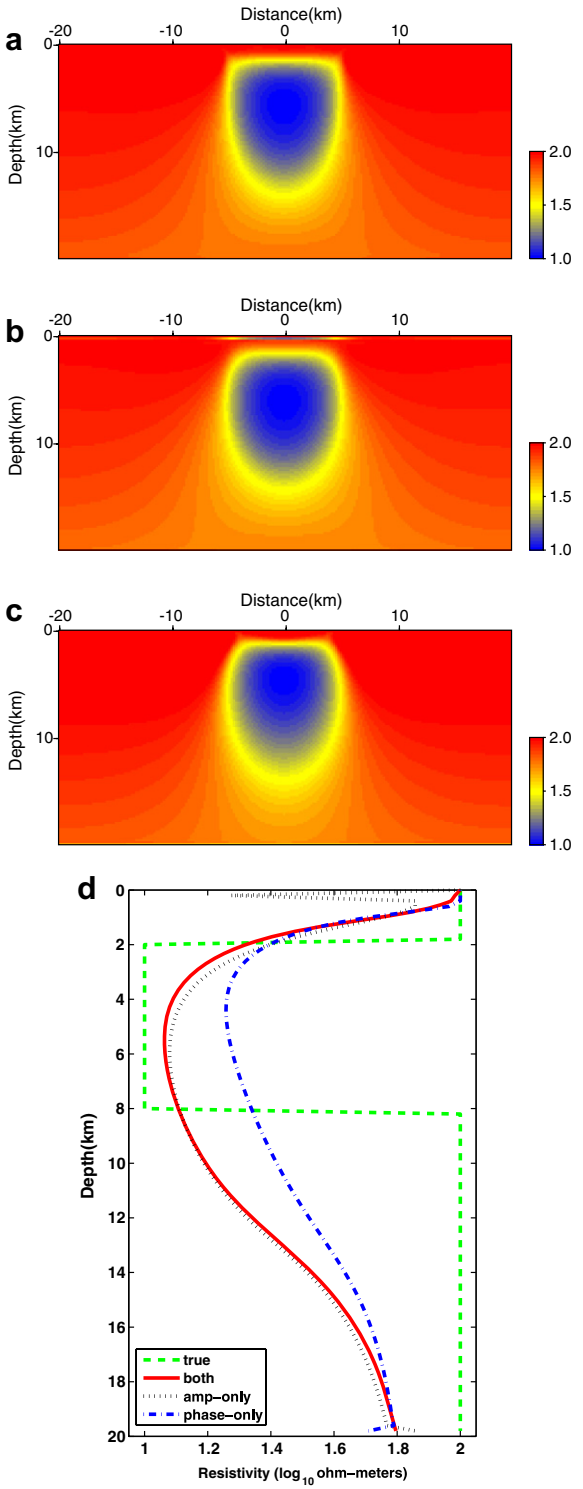

Fig. 5. Resistivity regions given by the inversion algorithm using resistivity cell of 200 m × 200 m (a) the inverted result using both amplitude and phase at 901th iteration, (b) the inverted result using amplitude only at 1101th iteration, (c) the inverted result using phase only at 1801th iteration, and, (d) the resistivity values extracted at the center of the surface. Resistivity scales have units $\log_{10}\Omega$-m.

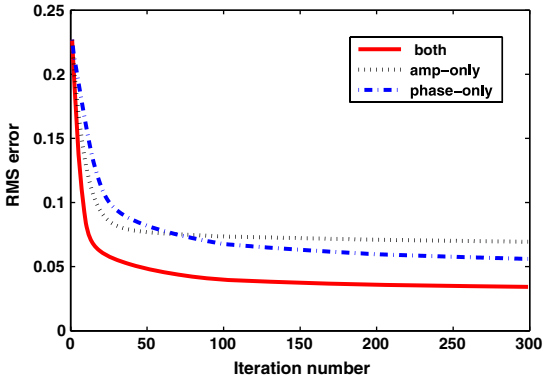

Fig. 6. History of RMS error for different inversion methods using cell parameterization in Model I. Solid line denotes history for RMS error of simultaneous inversion, dotted line denotes history for RMS error of amplitude only inversion and dash-dot line denotes history for RMS error of phase only inversion.

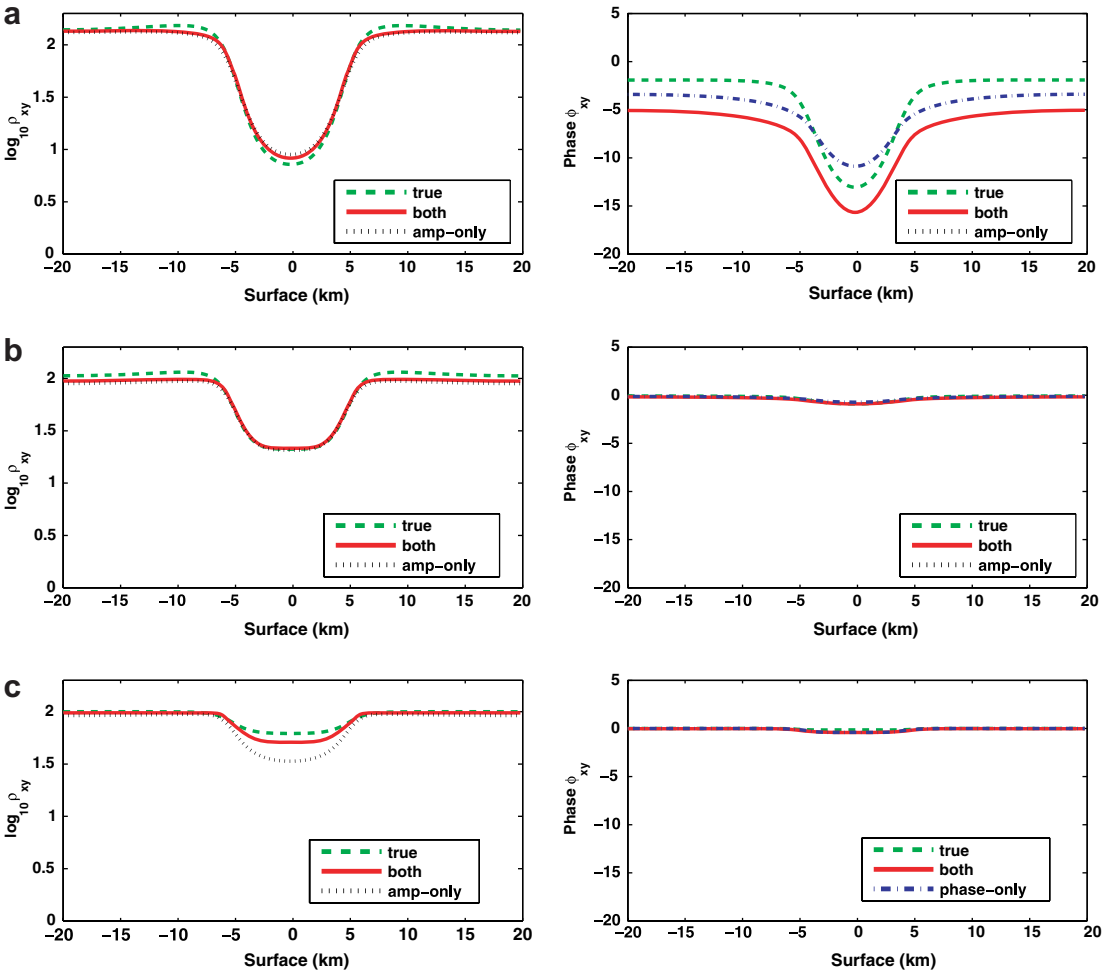

Fig. 7. Apparent resistivity and impedance phase in TM-mode using amplitude and phase, amplitude only and phase only method of inversion. Resistivity (ρ_{xy}) scale has units $\log_{10}\Omega$-m and phase (ϕ_{xy}) scale has units of Degree. (a) frequency at 0.01 Hz; (b) frequency at 1 Hz; and (c) frequency at 100 Hz.

100 Ω-m and 10 Ω-m, respectively, as shown in Fig. 4. For an initial model, we choose a homogeneous model of resistivity of 100 Ω-m, locate 81 receivers at the surface at an interval 200 m, and use 11 frequencies in the range 0.01–100 Hz evenly spaced on a logarithmic scale. The model parameterization for MT inversion divides

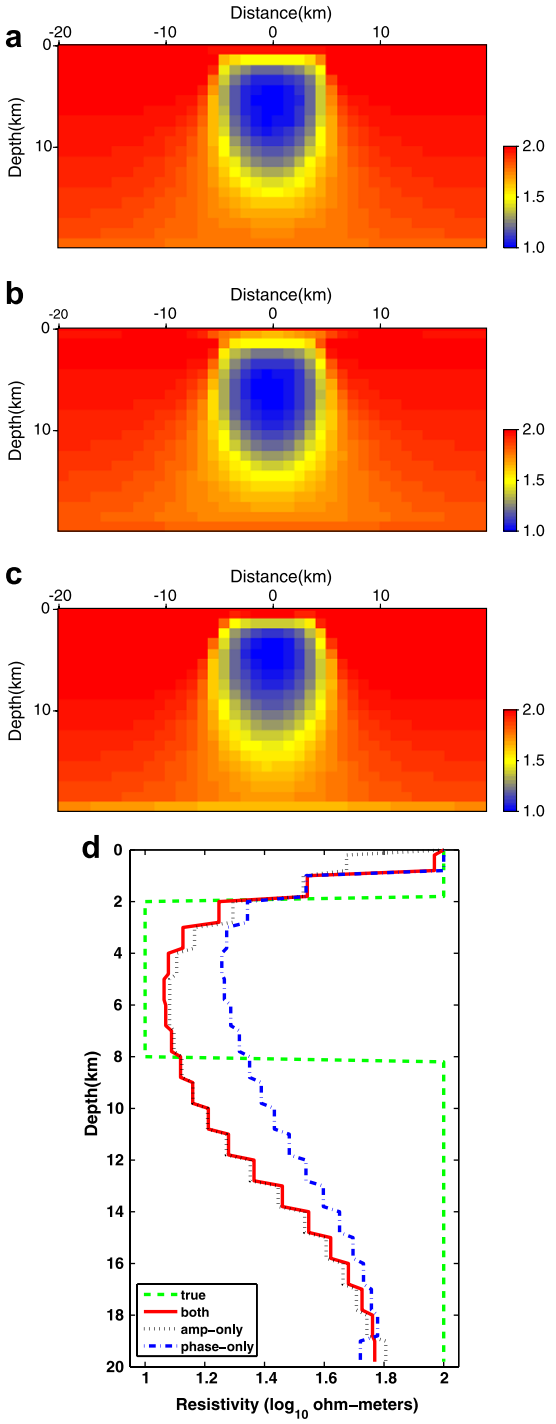

Fig. 8. Resistivity regions given by the inversion algorithm with the cell block of 1000 m × 1000 m (a) the inverted result using both amplitude and phase at 903th iteration, (b) the inverted result using amp-only at 1501th iteration, (c) the inverted result using phase-only at 1901th iteration, and, (d) the resistivity values extracted at the center of the surface. Resistivity scales have units $\log_{10}$ Ω-m.

the computational domain into a uniform grid. The number of grid points in the horizontal direction is 200 and that in the depth direction is 100. Therefore, we have 20,000 model parameters but when we use cell block (each block is 1000 m × 1000 m), we have 800 model parameters.

Figs. 5 and 8 show the results obtained by an inversion algorithm using the backpropagation technique with cells (each cell is 200 m × 200 m), and with cell blocks (each block is 1000 m × 1000 m), respectively. Figs. 5 and 8, (a), (b) and (c) represent the inverted image obtained from both amplitude and phase, amplitude-only and phase-only, respectively, and (d) shows the resistivity profile extracted at the center of the surface as a function of depth. From the inverted results, it is immediately obvious that the inverted image obtained by using both amplitude and phase is more similar to the true model than ones obtained using amplitude-only or phase-only. Moreover, from Figs. 5 and 8, we see that the inverted image for a small-size cell parameterization model shows smoother structure than the model with block parameterization, since the problem of cell parameterization has more unknowns than one with block parameterization. Figs. 6 and 9 display the graph of RMS errors for the inversion algorithms using three different objective functions. The RMS error for the objective function for both amplitude and phase is much smaller than that for the other two objective functions. We define the relative RMS error ratio of initial error to kth iteration error as $r(k)/r(1)$, where k is the smallest iteration number satisfying the stop criterion.

From Table 1, the relative RMS error for both amplitude and phase is smaller than that for other inversion algorithms. Figs. 7 and 10 show the residuals for amplitude and phase of complex apparent resistivity. The resistivity scale has units of $\log_{10}\Omega$-m and the unit of phase is Degree. At 0.01 Hz, 1 Hz and 100 Hz, we compare the residuals for the true model and for the inverted model. From Figs. 7 and 10, we observe that the residuals of amplitude are larger at higher frequency, but the residuals of phase are larger at lower frequency.

4.2. Model II: two rectangular blocks embedded in a homogeneous half space

The sizes of the surrounding homogeneous space and the two conductive blocks are 40 km × 20 km and 8 km × 6 km, respectively. The resistivity of the surrounding half space is 100 Ω-m, whereas the resistivity

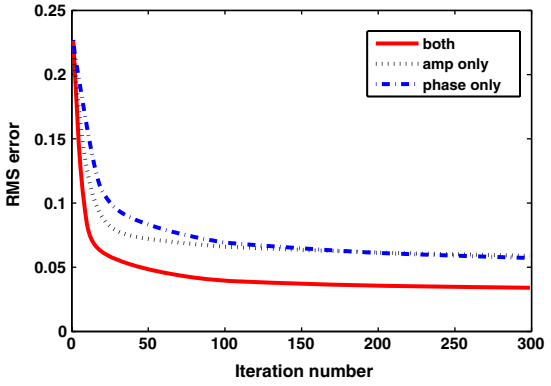

Fig. 9. History of RMS error for different inversion methods using block parameterization in Model I. Solid line denotes history for RMS error of simultaneous inversion, dotted line denotes history for RMS error of amplitude only inversion and dash-dot line denotes history for RMS error of phase only inversion.

Table 1
The relative rms error ration $r(k)/r(1)$ for the three models using the three objective functions

Type of objective function	Relative rms error ratio $r(k)/r(1)$					
	Both amplitude and phase		Amplitude only		Phase only	
Cell size	200 × 200	1000 × 1000	200 × 200	1000 × 1000	200 × 200	1000 × 1000
Model I	12.9%	12.8%	27.8%	21.9%	19.3%	19.4%
Model II	13.4%	13.7%	30.3%	23.5%	21.0%	21.0%
Model III	5.68%	5.36%	8.96%	8.32%	8.68%	8.47%

Here, k is the smallest number of iterations which satisfied the stop criterion.

of the left conductive body is 20 Ω-m and the resistivity of the right conductivity body is 10 Ω-m. We choose the model that places both buried conductive bodies at same depth 2 km as shown in Fig. 11. We locate 81 receivers at the surface at an interval 200 m, and use 31 frequencies that range from 0.01 to 100 Hz evenly spaced on a logarithmic scale.

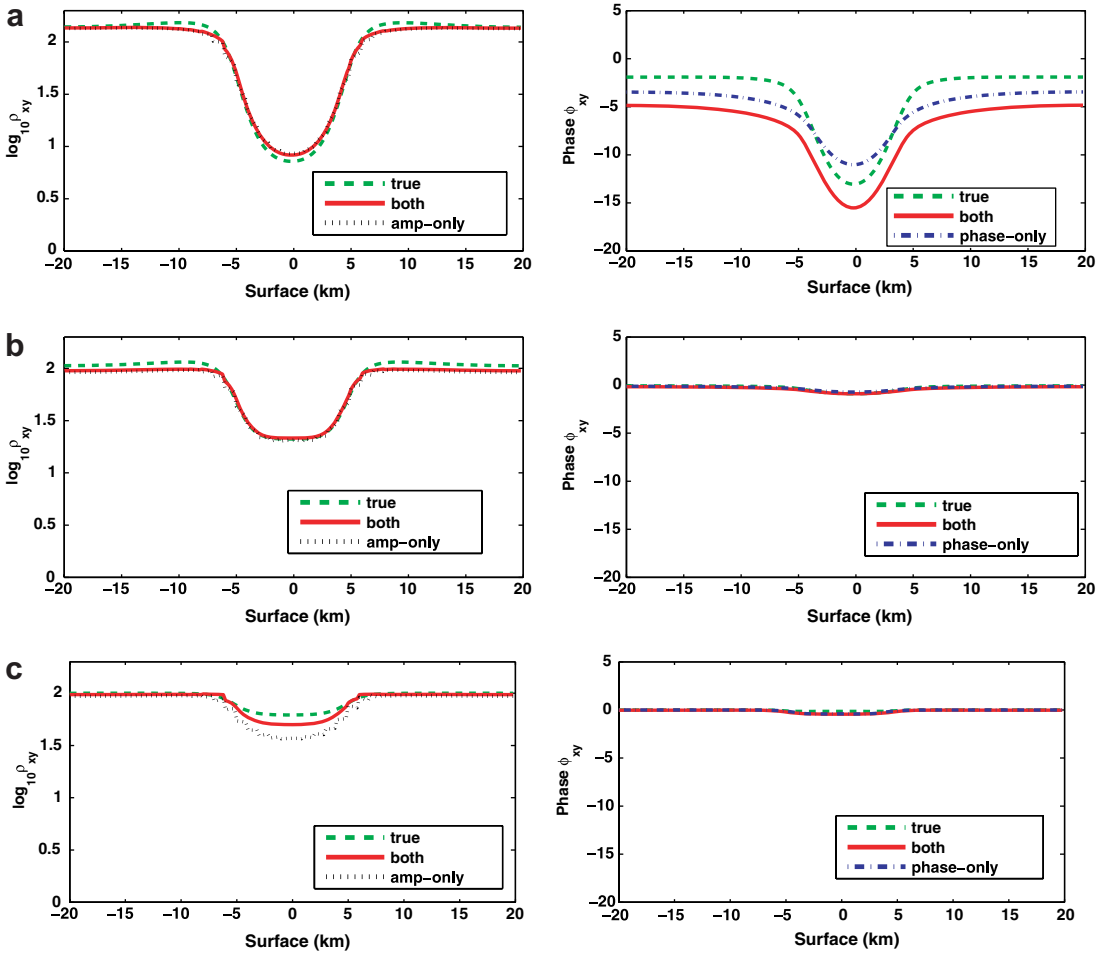

Fig. 10. Apparent resistivity and impedance phase in TM-mode using amplitude and phase, amplitude only and phase only method of inversion. Resistivity (ρ_{xy}) scale has units $\log_{10}$ Ω-m and phase (ϕ_{xy}) scale has units of Degree: (a) frequency at 0.01 Hz; (b) frequency at 1 Hz; and (c) frequency at 100 Hz.

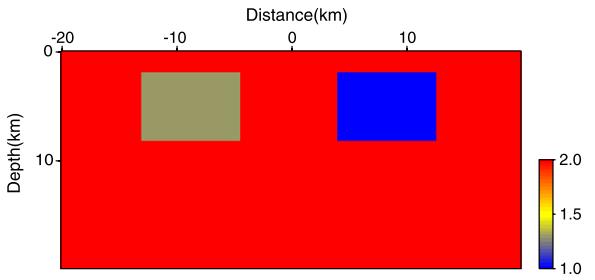

Fig. 11. 2-D true model used for resistivity inversion where both buried conductive block are located starting at 2 km depth from the earth surface. Resistivity scale has units $\log_{10}$ Ω-m.

For an initial model for numerical test, we choose a homogeneous model of resistivity of 100 Ω-m. Figs. 12 and 15 show the results obtained by an inversion algorithm for cells and cell blocks, respectively. Figs. 12 and

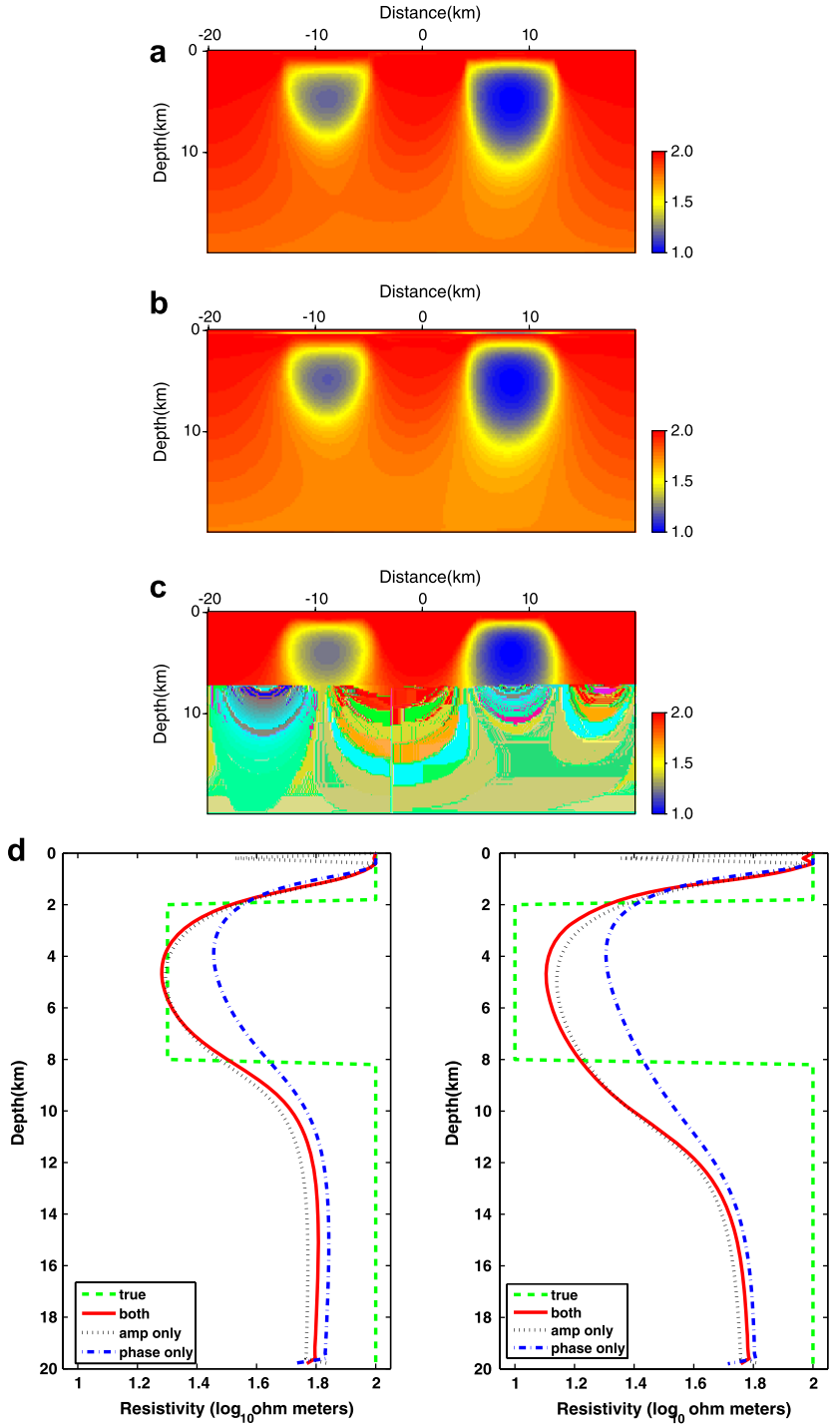

Fig. 12. Resistivity regions given by the inversion algorithm with the cell block of 200 m × 200 m: (a) the inverted result using both amplitude and phase at 1901th iteration, (b) the inverted result using amp-only at 903th iteration, (c) the inverted result using phase-only at 1501th iteration, and, (d) the resistivity extracted at −8 km (left) and 8 km (right) points on the surface as function of depth. Resistivity scales have units $\log_{10}$ Ω-m.

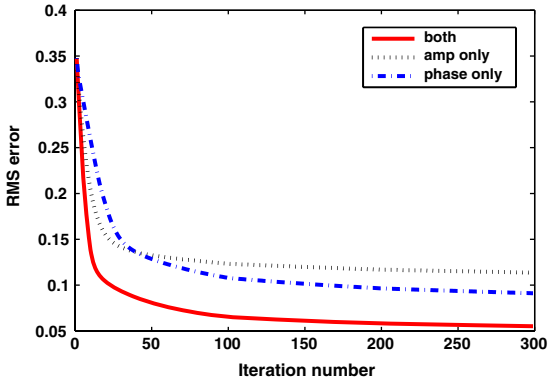

Fig. 13. History of RMS error for different inversion methods using cell parameterization in Model II. Solid line denotes history for RMS error of simultaneous inversion, dotted line denotes history for RMS error of amplitude only inversion and dash-dot line denotes history for RMS error of phase only inversion.

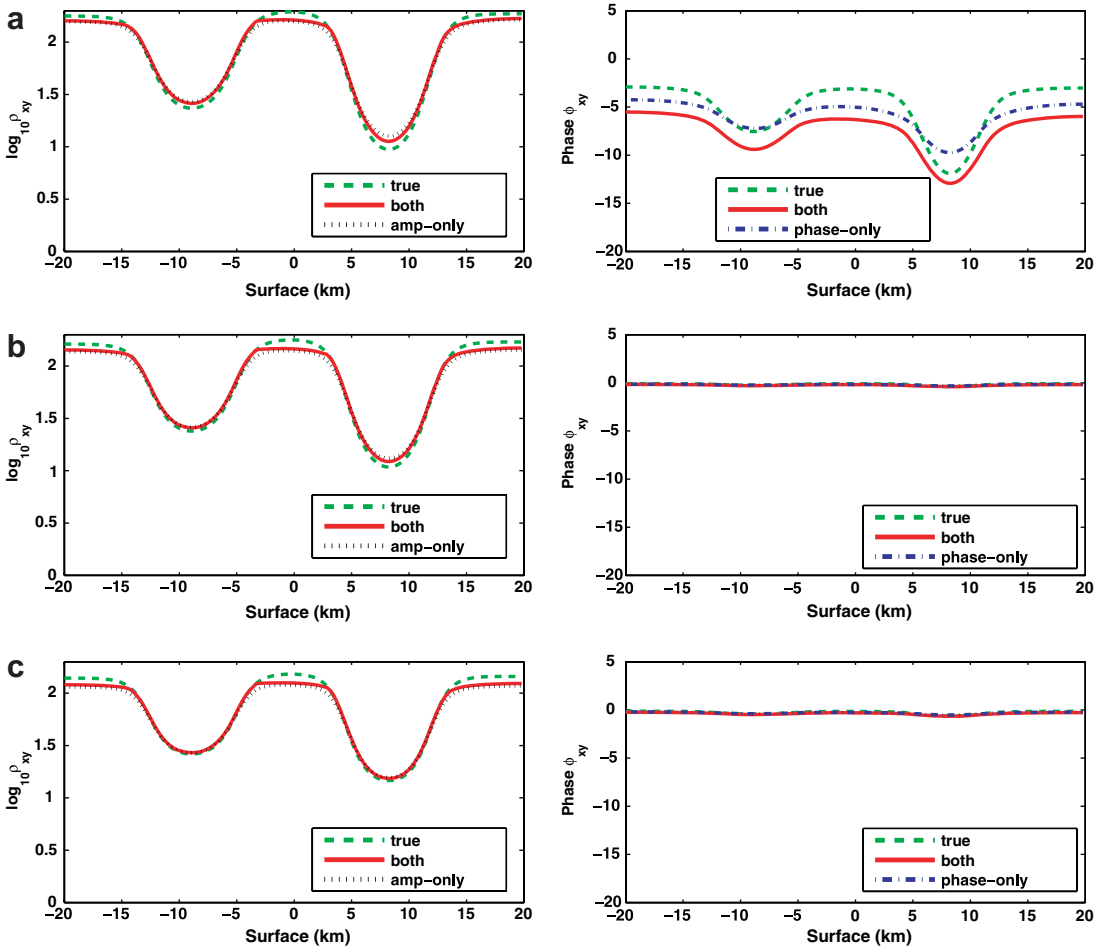

Fig. 14. Apparent resistivity and impedance phase in TM-mode using amplitude and phase, amplitude only and phase only method of inversion. Resistivity (ρ_{xy}) scale has units $\log_{10}\Omega$-m and phase (ϕ_{xy}) scale has units of Degree: (a) frequency at 0.01 Hz; (b) frequency at 1 Hz; and (c) frequency at 100 Hz.

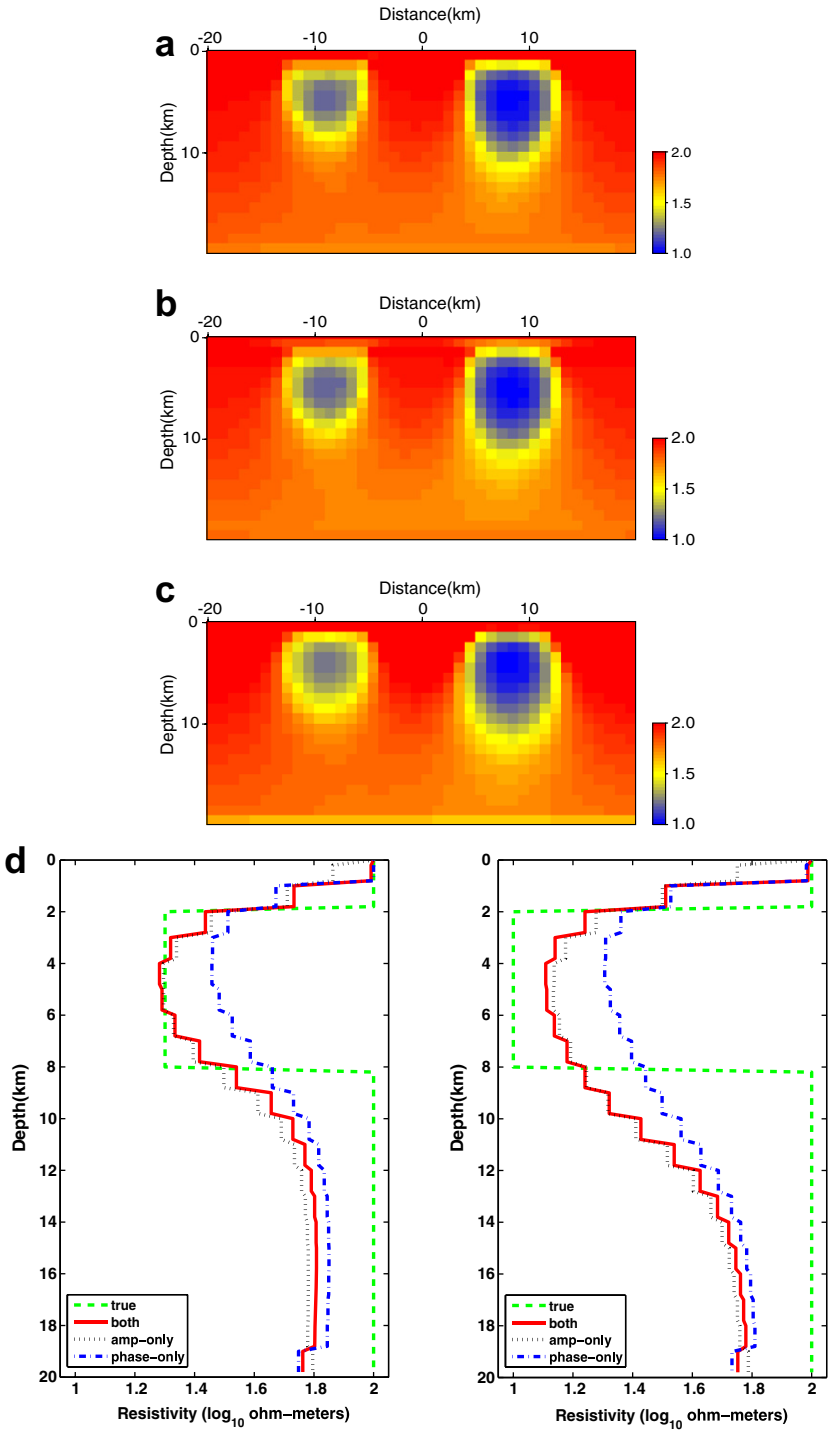

Fig. 15. Resistivity regions given by the inversion algorithm with the cell block of 1000 m × 1000 m: (a) the inverted result using both amplitude and phase at 1101th iteration, (b) the inverted result using amp-only at 150th iteration, (c) the inverted result using phase-only at 1901th iteration, and, (d) the resistivity extracted at −8 km (left) and 8 km (right) points on the surface as function of depth. Resistivity scales have units $\log_{10}\Omega$-m.

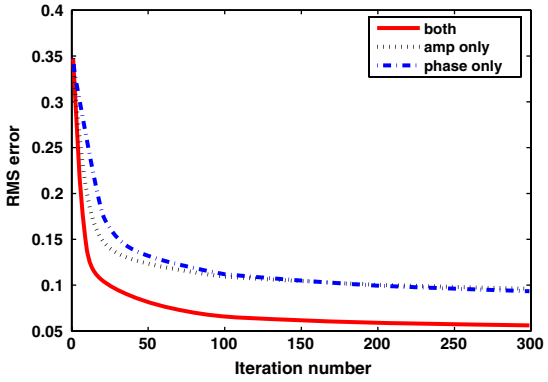

Fig. 16. History of RMS error at each different inversion methods using block parameterization in Model II. Solid line denotes history for RMS error of simultaneous inversion, dotted line denotes history for RMS error of amplitude only inversion and dash-dot line denotes history for RMS error of phase only inversion.

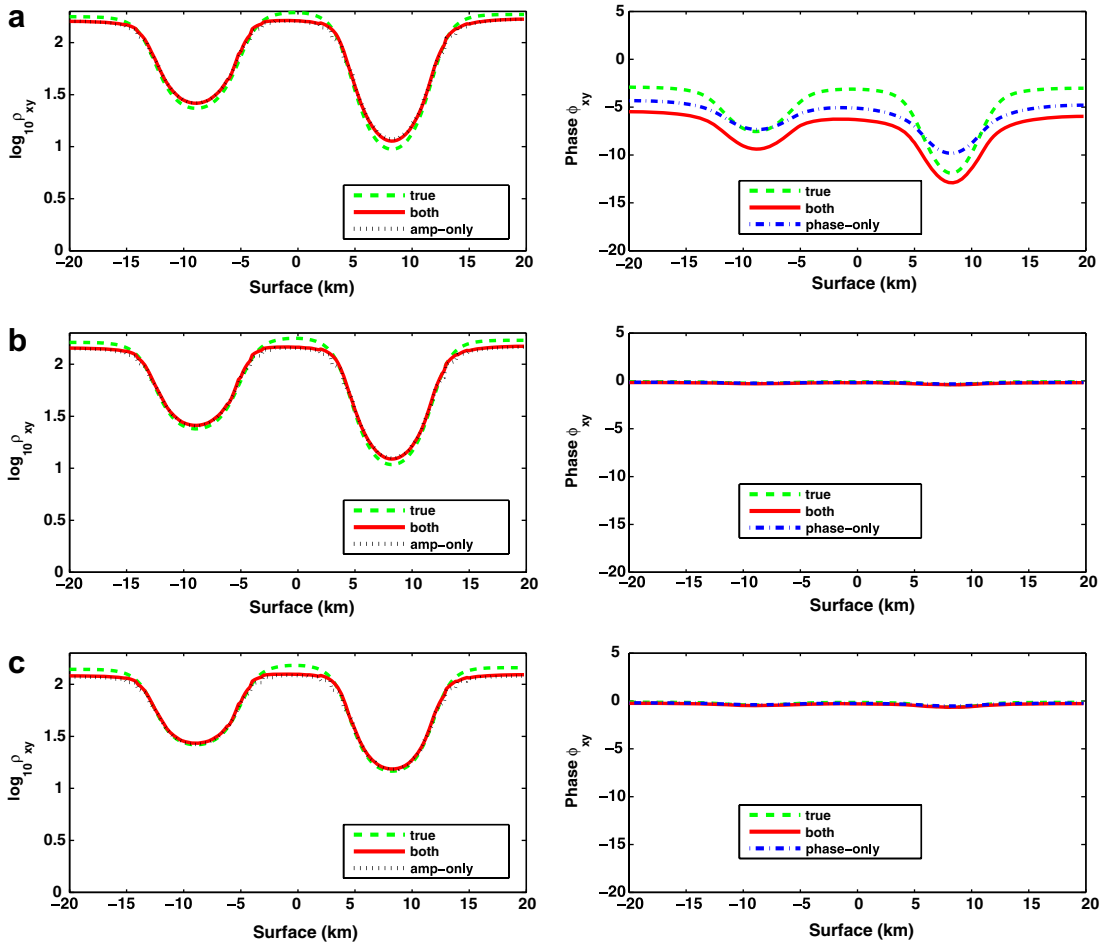

Fig. 17. Apparent resistivity and impedance phase in TM-mode using amplitude and phase, amplitude only and phase only method of inversion. Resistivity (ρ_{xy}) scale has units $\log_{10}\Omega$-m and phase (ϕ_{xy}) scale has units of Degree: (a) frequency at 0.01 Hz; (b) frequency at 1 Hz; and (c) frequency at 100 Hz.

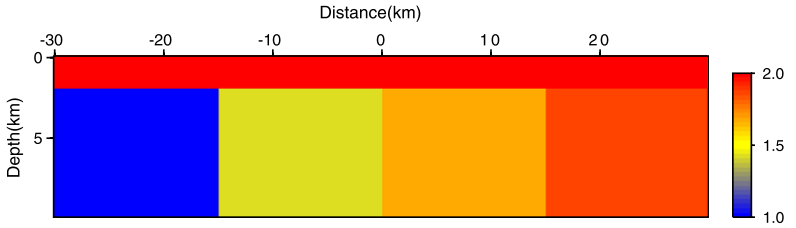

Fig. 18. The model size is 60 km × 10 km. The model consists of conductive blocks buried in Earth. The resistivity from 2 km depth is 100 Ω-m. Below the depth of 2 km, the resistivities for four regions from left to right are 20, 40, 60 and 80 Ω-m, respectively. Resistivity scale has units $\log_{10}$ Ω-m.

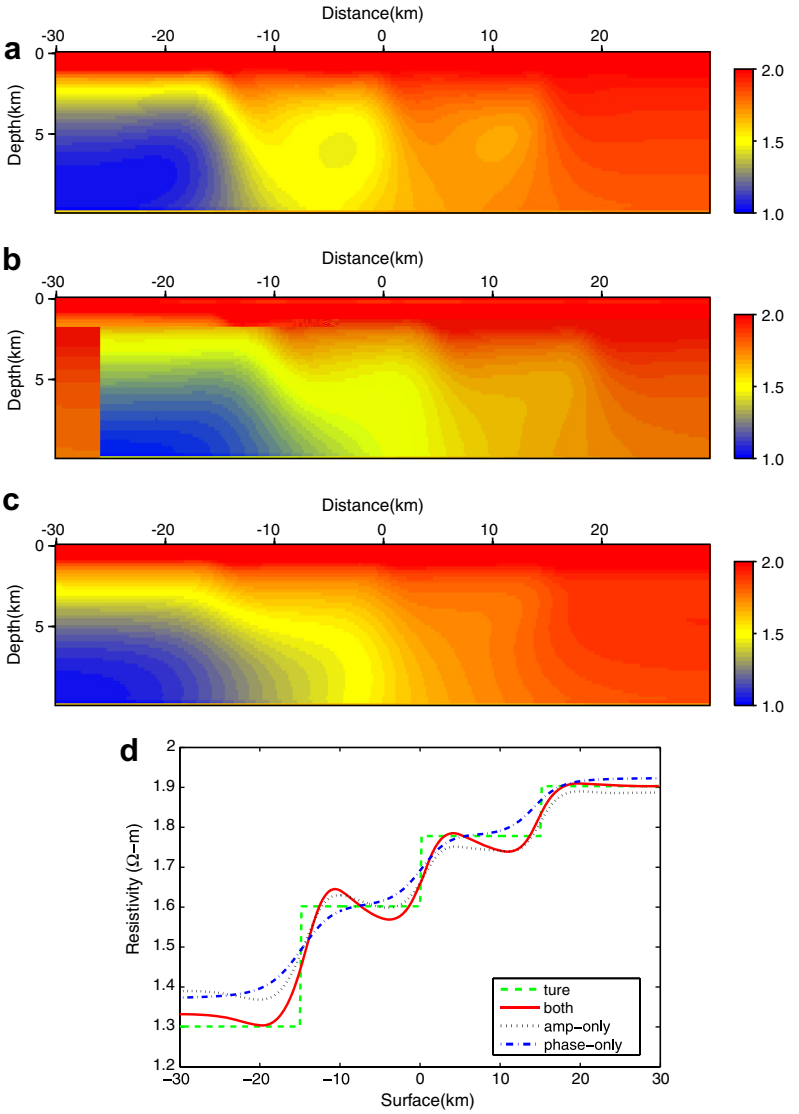

Fig. 19. Resistivity regions given by the inversion algorithm with the cell block of 200 m × 200 m: (a) the inverted result using both amplitude and phase at 201th iteration, (b) the inverted result using amp-only at 1501th iteration, (c) the inverted result using phase-only at 379th iteration, and, (d) the resistivity extracted at 5 km along the depth. Resistivity scales have units $\log_{10}$ Ω-m.

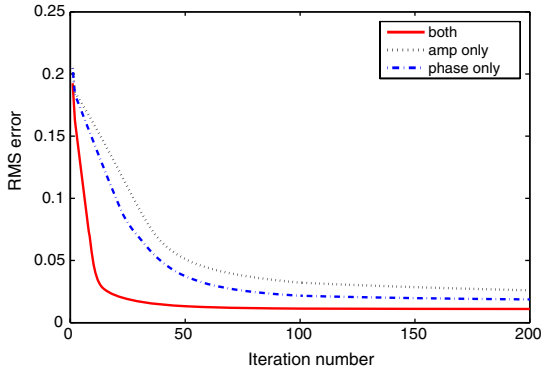

Fig. 20. History of RMS error for each different inversion methods using cell parameterization in Model III. Solid line denotes history for RMS error of simultaneous inversion, dotted line denotes history for RMS error of amplitude only inversion and dash-dot line denotes history for RMS error of phase only inversion.

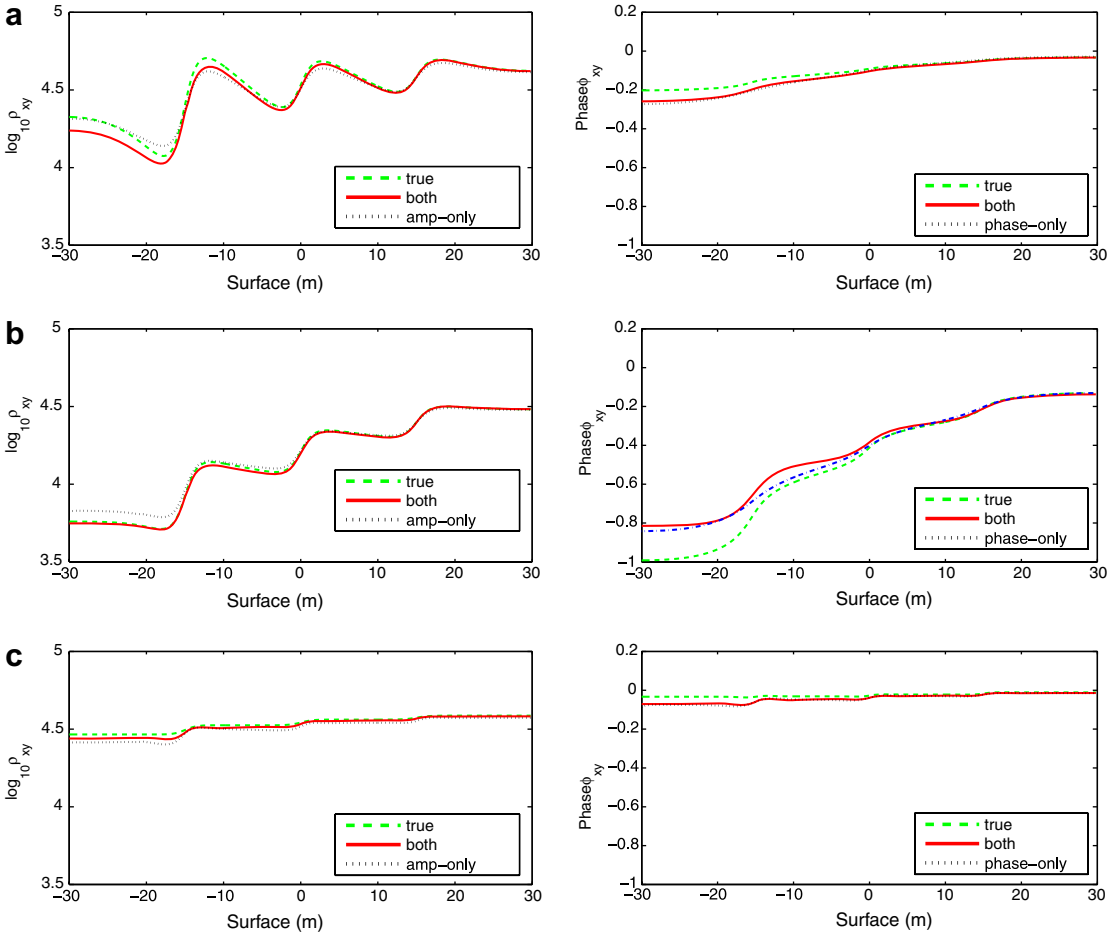

Fig. 21. Apparent resistivity and impedance phase in TM-mode using amplitude and phase, amplitude only and phase only method of inversion. Resistivity (ρ_{xy}) scale has units $\log_{10}\Omega$-m and phase (ϕ_{xy}) scale has units of Degree: (a) frequency at 0.01 Hz (b) frequency at 1 Hz; and (c) frequency at 100 Hz.

15(a), (b) and (c) represent the inverted images for both amplitude and phase, amplitude-only and phase-only, respectively, while Figs. 12 and 15(d) show the resistivity profile extracted at 8 km and −8 km points on the surface as function of depth. From Figs. 12 and 15(d), we know that the resistivity profile of the anomaly with higher resistivity is easier to recover than that of the anomaly with lower resistivity.

From Figs. 12 and 15, we can confirm again that the cell parameterization results in obtaining a smoother recovered structure than block parameterization since the problem with the cell parameterization has more unknowns than one with the block parameterization since the problem with the cell parameterization has more unknowns than one with the block parameterization. From the inverted results, it is clear that the inverted image obtained using both amplitude and phase converges better to the original image than that obtained using amplitude-only or phase-only. Figs. 13 and 16 display the graph of history of RMS errors for inversion algorithms using three different types of objective functions. As observed in Model I test, the RMS error for the objective function of both amplitude and phase is the smallest one among the three different objective functions.

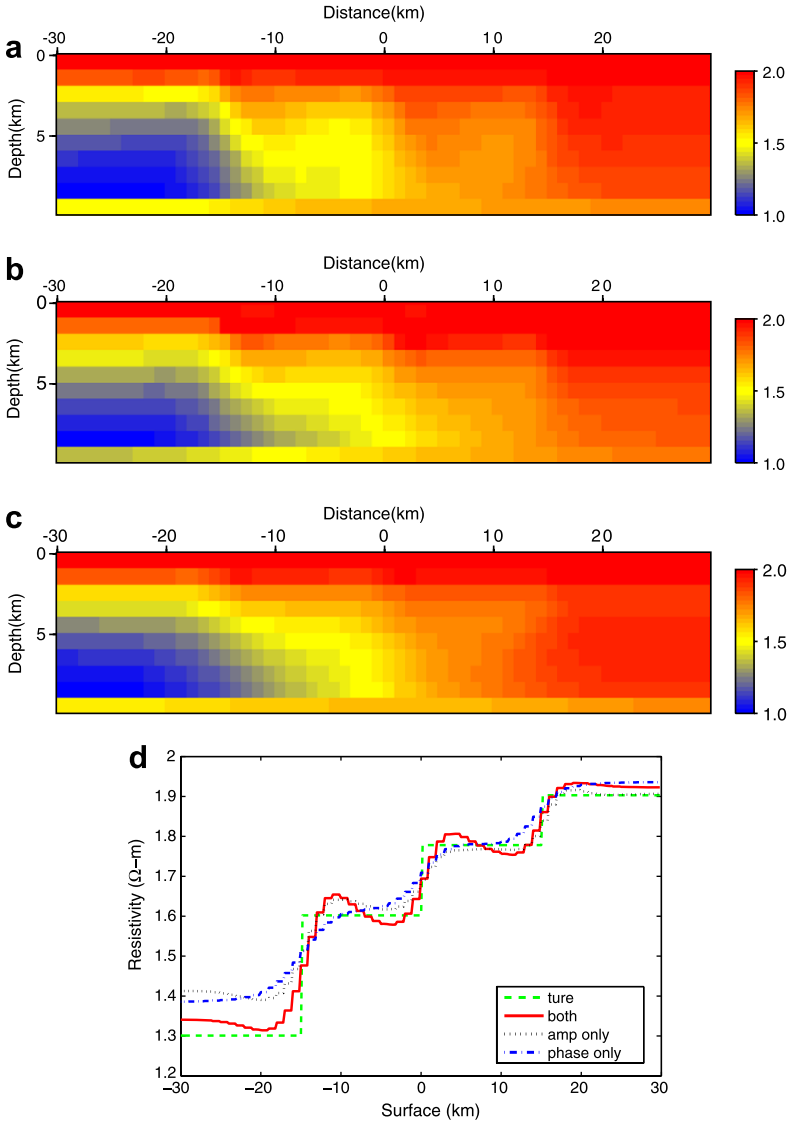

Fig. 22. Resistivity regions given by the inversion algorithm with the cell block of 1000 m × 1000 m: (a) the inverted result using both amplitude and phase at 207th iteration, (b) the inverted result using amp-only at 801th iteration, (c) the inverted result using phase-only at 501th iteration, and, (d) the resistivity extracted at 5 km along the depth. Resistivity scales have units $\log_{10}$ Ω-m.

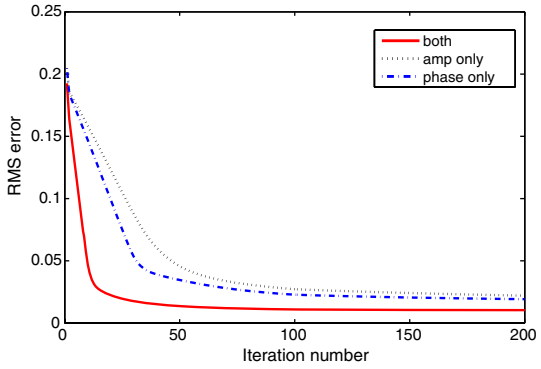

Fig. 23. History of RMS error for each different inversion methods using cell parameterization in Model III. Solid line denotes history for RMS error of simultaneous inversion, dotted line denotes history for RMS error of amplitude only inversion and dash-dot line denotes history for RMS error of phase only inversion.

From Table 1, the relative RMS error ratio for inversion algorithm using both amplitude and phase is smaller than that using other inversion algorithms. Figs. 14 and 17 show the residual of amplitude and phase of complex apparent resistivity. At 0.01 Hz, 1 Hz and 100 Hz, we compare the residuals for the true model

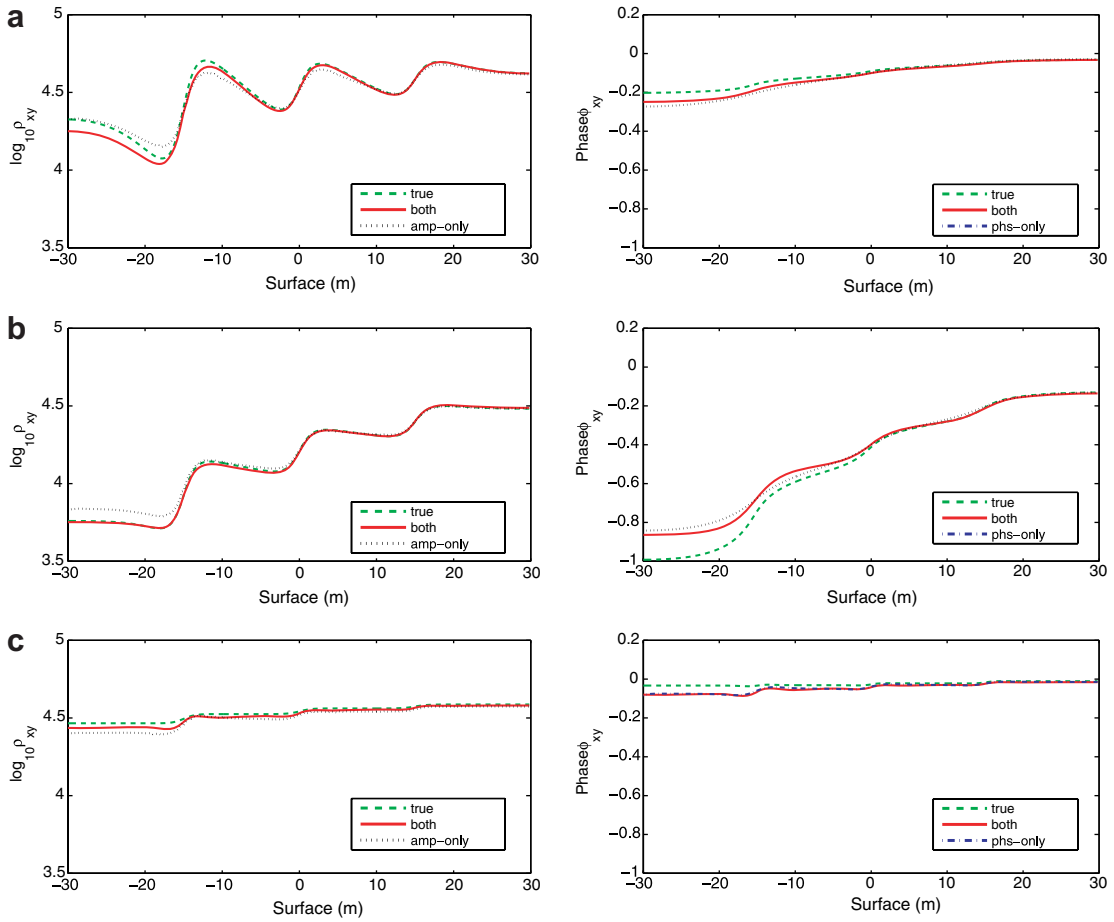

Fig. 24. Apparent resistivity and impedance phase in TM-mode using amplitude and phase, amplitude only and phase only method of inversion. Resistivity (ρ_{xy}) scale has units $\log_{10}\Omega$-m and phase (ϕ_{xy}) scale has units of Degree: (a) frequency at 0.01 Hz; (b) frequency at 1 Hz; and (c) frequency at 100 Hz.

and the inverted model. From the results of Figs. 14 and 17, we observe that the residuals of amplitude are almost same at higher frequency, but the residuals of phase are larger at lower frequency.

4.3. Model III: complex rectangular blocks in a half space

The size of the surrounding homogeneous space is 60 km × 10 km. The resistivity up to 2 km depth is 100 Ω-m, and below the depth 2 km, the resistivities of the four regions (which extend from 2 km to 10 km depth) from left to right are 20, 40, 60 and 80 Ω-m, respectively (see Fig. 18). We locate 290 receivers at the surface with an interval 200 m, and use 15 frequencies that range from 0.01 to 100 Hz evenly spaced on a logarithmic scale.

For an initial model for numerical test, we choose a homogeneous model of resistivity of 100 Ω-m. Figs. 19 and 22 show the results obtained by an inversion algorithm using cells and cell blocks, respectively. Figs. 19 and 22(a), (b) and (c) represent the inverted images for both amplitude and phase, amplitude-only and phase-only, respectively, while Figs. 19 and 22(d) show the resistivity profile extracted at a depth of 5 km. In Figs. 19 and 22(d), we see that at the lowest resistivity anomaly, the resistivity obtained using both amplitude and phase is closest to the original resistivity among inversions with the three objective functions. Figs. 20 and 23 display the graph of history of RMS errors for inversion algorithms using three different types of objective functions. As observed in Model I and II tests, the RMS error for the objective function of both amplitude and phase is the smallest one among three different objective functions.

From Table 1, the relative RMS error ratio for inversion algorithm using both amplitude and phase is smaller than that using other inversion algorithms. Figs. 21 and 24 show the residual of amplitude and phase of complex apparent resistivity. At 0.01 Hz, 1 Hz and 100 Hz, we compare the residuals for the true model and the inverted model. From the results of Figs. 21 and 24, we know that the residuals of both amplitude and phase are more sensitive at 1 Hz.

5. Conclusion

In this paper, instead of defining the objective function as l_2 norm with apparent resistivity, we construct an objective functions with logarithm of complex apparent resistivity. Our logarithmic technique enables us to perform the inversion to obtain the amplitude of the apparent resistivity, or the phase of the apparent resistivity, or both simultaneously. The objective functions are separated into three types, and are constructed using amplitude-only, phase-only and both amplitude and phase of complex apparent resistivity.

We calculate the steepest descent direction for each of the three types of objective functions without computing the Jacobian matrix explicitly. The steepest descent direction is obtained by the backpropagation technique combined with inner product between the virtual source and backpropagated residuals. Our algorithm backpropagates the residual vector defined as the logarithm of the ratio of the modeled apparent resistivity and the observed apparent resistivity measured in the field, instead of backpropagating the residual of apparent resistivity. Therefore, our algorithm share features of the seismic algorithm proposed by Shin and Min [22].

The advantage of our algorithm lies in the fact that we do not have multiple right-hand side vectors in MT forward modeling, which arises in multiple source problems such as dc, EM and seismic experiments. Once we factor the resulting impedance matrix, we can efficiently compute the steepest descent direction by simple backward and forward substitutions of the already factored impedance matrix without incurring extra computational cost. From three numerical experiments, we see that inversion with the cell by cell parameterization produces smoother image than the inversion with block parameterization. Moreover, we confirm that the inversion with simultaneous use of amplitude and phase produce the best resolution in our synthetic models.

We have proposed the MT inversion under the modeling of TM-mode. For the MT inversion theory under the modeling of TE-mode, we can extend the theory without any difficulty. In the future, we plan to apply MT inversion to anisotropic media. Of course, we feel that the conjugate-gradient method used in the inversion significantly reduces the computation time.

Acknowledgments

The work of T. Ha was supported by the Korea Research Foundation Grant (KRF-2006-C00014) and the work of C. Shin was financially supported by the Brain Korea 21 Project of the Korea Ministry of Education.

Appendix A. Proof of Eq. (17)

For each frequency ω, we can express the electric field vector as

$$E_x(\omega) = e_x(\omega)\exp(\mathrm{i}\theta_E(\omega)), \tag{A.1a}$$
$$E_z(\omega) = e_z(\omega)\exp(\mathrm{i}\theta_E(\omega)), \tag{A.1b}$$
$$H_y(\omega) = h_y(\omega)\exp(\mathrm{i}\theta_H(\omega)), \tag{A.1c}$$

where e_x, e_z, h_y are the amplitudes, and θ_E and θ_H are the phases. Similarly, the measured field vectors at the surface can be expressed as

$$E_x^d(\omega) = e_x^d(\omega)\exp(\mathrm{i}\theta_E^d(\omega)), \tag{A.2a}$$
$$E_z^d(\omega) = e_z^d(\omega)\exp(\mathrm{i}\theta_E^d(\omega)), \tag{A.2b}$$
$$H_y^d(\omega) = h_y^d(\omega)\exp(\mathrm{i}\theta_H^d(\omega)). \tag{A.2c}$$

Dividing Eq. (A.2) by Eq. (A.1) and taking the logarithm gives

$$\ln\left[\frac{E_x}{E_x^d}\right] = \ln\left[\frac{e_x}{e_x^d}\right] + \mathrm{i}\left[\theta_E - \theta_E^d\right], \tag{A.3a}$$
$$\ln\left[\frac{E_z}{E_z^d}\right] = \ln\left[\frac{e_z}{e_z^d}\right] + \mathrm{i}\left[\theta_E - \theta_E^d\right], \tag{A.3b}$$
$$\ln\left[\frac{H_y}{H_y^d}\right] = \ln\left[\frac{h_y}{h_y^d}\right] + \mathrm{i}\left[\theta_H - \theta_H^d\right]. \tag{A.3c}$$

Differentiating Eq. (A.1) with respect to p_k we have

$$\frac{\partial E_x}{\partial p_k} = \frac{\partial e_x}{\partial p_k}\exp(\mathrm{i}\theta_E) + \mathrm{i}e_x\exp(\mathrm{i}\theta_E)\frac{\partial \theta_E}{\partial p_k}, \tag{A.4a}$$
$$\frac{\partial E_z}{\partial p_k} = \frac{\partial e_z}{\partial p_k}\exp(\mathrm{i}\theta_E) + \mathrm{i}e_z\exp(i\theta_E)\frac{\partial \theta_E}{\partial p_k}, \tag{A.4b}$$
$$\frac{\partial H_y}{\partial p_k} = \frac{\partial h_y}{\partial p_k}\exp(\mathrm{i}\theta_H) + \mathrm{i}h_y\exp(\mathrm{i}\theta_H)\frac{\partial \theta_H}{\partial p_k}. \tag{A.4c}$$

Dividing Eq. (A.4) by Eq. (A.1) gives

$$\frac{1}{E_x}\frac{\partial E_x}{\partial p_k} = \frac{1}{e_x}\frac{\partial e_x}{\partial p_k} + \mathrm{i}\frac{\partial \theta_E}{\partial p_k}, \tag{A.5a}$$
$$\frac{1}{E_z}\frac{\partial E_z}{\partial p_k} = \frac{1}{e_z}\frac{\partial e_z}{\partial p_k} + \mathrm{i}\frac{\partial \theta_E}{\partial p_k}, \tag{A.5b}$$
$$\frac{1}{H_y}\frac{\partial H_y}{\partial p_k} = \frac{1}{h_y}\frac{\partial h_y}{\partial p_k} + \mathrm{i}\frac{\partial \theta_H}{\partial p_k}. \tag{A.5c}$$

We can see easily that Eq. (A.5) implies Eq. (17).

Appendix B. Theory of inversion with objective function defined by amplitude-only or phase-only

We define the objective function Ψ using logarithm amplitude ratio only as

$$\Psi(\mathbf{p}) = \frac{1}{2}\sum_{j_\omega=1}^{N_\omega}\sum_{j_r=1}^{N_r}\left[\ln\frac{\rho_{xy}^{j_r}}{\rho_{xy}^{d,j_r}}\right]^2. \tag{B.1}$$

Taking derivative of the objective function given by Eq. (B.1) yields

$$\begin{aligned}\nabla_{p_k}\boldsymbol{\Psi} &= \sum_{j_\omega=1}^{N_\omega}\sum_{j_r=1}^{N_r}\left[\ln\frac{\rho_{xy}^{j_r}}{\rho_{xy}^{d,j_r}}\frac{\partial}{\partial p_k}\left(\ln\frac{\rho_{xy}^{j_r}}{\rho_{xy}^{d,j_r}}\right)\right] = 2\sum_{j_\omega=1}^{N_\omega}\sum_{j_r=1}^{N_r}\left[\mathbf{Re}\left(r_{xy}^{j_r}\right)\mathbf{Re}\left(\frac{1}{E_x^{j_r}}\frac{\partial E_x^{j_r}}{\partial p_k}-\frac{1}{H_y^{j_r}}\frac{\partial H_y^{j_r}}{\partial p_k}\right)\right]\\ &= 2\sum_{j_\omega=1}^{N_\omega}\sum_{j_r=1}^{N_r}\mathbf{Re}\left[\frac{\partial E_x^{j_r}}{\partial p_k}\frac{1}{E_x^{j_r}}\mathbf{Re}\left(r_{xy}^{j_r}\right)-\frac{\partial H_y^{j_r}}{\partial p_k}\frac{1}{H_y^{j_r}}\mathbf{Re}\left(r_{xy}^{j_r}\right)\right] = 2\sum_{j_\omega=1}^{N_\omega}\sum_{j_r=1}^{N_r}\mathbf{Re}\left(\begin{bmatrix}\frac{\partial E_x^{j_r}}{\partial p_k} & \frac{\partial H_y^{j_r}}{\partial p_k}\end{bmatrix}\begin{bmatrix}\frac{1}{E_x^{j_r}}\mathbf{Re}\left(r_{xy}^{j_r}\right)\\ -\frac{1}{H_y^{j_r}}\mathbf{Re}\left(r_{xy}^{j_r}\right)\end{bmatrix}\right).\end{aligned} \tag{B.2}$$

Therefore,

$$\nabla_{p_k}\boldsymbol{\Psi} = \mathbf{Re}\sum_{j_\omega=1}^{N_\omega}\left(\frac{\partial\mathbf{u}^{\mathrm{T}}}{\partial p_k}\tilde{\mathbf{r}}_{\mathrm{B}}+\frac{\partial\mathbf{u}^{\mathrm{T}}}{\partial p_k}\tilde{\mathbf{r}}_{\mathrm{T}}\right), \tag{B.3}$$

where $\tilde{\mathbf{r}}_{\mathrm{B}}$ or $\tilde{\mathbf{r}}_{\mathrm{T}}$ are

$$\left[\frac{1}{E_x^1}\mathbf{Re}\left(r_{xy}^1\right)\cdots\frac{1}{E_x^{N_r}}\mathbf{Re}\left(r_{xy}^{N_r}\right)0\cdots0\frac{-1}{H_y^1}\mathbf{Re}\left(r_{xy}^1\right)\cdots\frac{-1}{H_y^{N_r}}\mathbf{Re}\left(r_{xy}^{N_r}\right)0\cdots0\right]^{\mathrm{T}}. \tag{B.4}$$

Similarly, for inversion with phase-only, we define the objective function using phase of complex apparent resistivity as

$$\Psi(\mathbf{p}) = \frac{1}{2}\sum_{j_\omega=1}^{N_\omega}\sum_{j_r=1}^{N_r}\left[\left(\phi_{xy}^{j_r}-\phi_{xy}^{d,j_r}\right)^2\right]. \tag{B.5}$$

The partial derivative of the objective function given by Eq. (B.5) becomes

$$\nabla_{p_k}\boldsymbol{\Psi} = 2\sum_{j_\omega=1}^{N_\omega}\sum_{j_r=1}^{N_r}\mathbf{Im}\left(\begin{bmatrix}\frac{\partial E_x^{j_r}}{\partial p_k} & \frac{\partial H_y^{j_r}}{\partial p_k}\end{bmatrix}\begin{bmatrix}\frac{1}{E_x^{j_r}}\mathbf{Im}\left(r_{xy}^{j_r}\right)\\ -\frac{1}{H_y^{j_r}}\mathbf{Im}\left(r_{xy}^{j_r}\right)\end{bmatrix}\right) = 2\sum_{j_\omega=1}^{N_\omega}\sum_{j_r=1}^{N_r}\mathbf{Re}\left(-\mathrm{i}\begin{bmatrix}\frac{\partial E_x^{j_r}}{\partial p_k} & \frac{\partial H_y^{j_r}}{\partial p_k}\end{bmatrix}\begin{bmatrix}\frac{1}{E_x^{j_r}}\mathbf{Im}\left(r_{xy}^{j_r}\right)\\ -\frac{1}{H_y^{j_r}}\mathbf{Im}\left(r_{xy}^{j_r}\right)\end{bmatrix}\right).$$

Therefore,

$$\nabla_{p_k}\boldsymbol{\Psi} = \mathbf{Re}\sum_{j_\omega=1}^{N_\omega}\left(\frac{\partial\mathbf{u}^{\mathrm{T}}}{\partial p_k}\tilde{\mathbf{r}}_{\mathrm{B}}+\frac{\partial\mathbf{u}^{\mathrm{T}}}{\partial p_k}\tilde{\mathbf{r}}_{\mathrm{T}}\right), \tag{B.6}$$

where $\tilde{\mathbf{r}}_{\mathrm{B}}$ or $\tilde{\mathbf{r}}_{\mathrm{T}}$ can be expressed by

$$\left[\frac{-\mathrm{i}}{E_x^1}\mathbf{Im}\left(r_{xy}^1\right)\cdots\frac{-\mathrm{i}}{E_x^{N_r}}\mathbf{Im}\left(r_{xy}^{N_r}\right)0\cdots0\frac{\mathrm{i}}{H_y^1}\mathbf{Im}\left(r_{xy}^1\right)\cdots\frac{\mathrm{i}}{H_y^{N_r}}\mathbf{Im}\left(r_{xy}^{N_r}\right)0\cdots0\right]^{\mathrm{T}}. \tag{B.7}$$

References

[1] W. Bangerth, R. Hartmann, G. Kanschat, deal.II Differential Equations Analysis Library, Technical Reference. IWR, Universität Heidelberg, <http://www.dealii.org>.

[2] T. Ha, S. Pyun, C. Shin, Efficient electric resistivity inversion using adjoint state of mixed finite-element method for Poisson equation, J. Comput. Phys. 214 (2006) 171–186.
[3] T. Ha, S. Seo, D. Sheen, Parallel iterative procedures for a computational electromagnetic modeling based on a nonconforming mixed finite element method, CMES 14 (1) (2006) 57–76.
[4] G.J. Hicks, R.G. Pratt, Reflection waveform inversion using local descent methods: numerical results, Geophysics 51 (2001) 1387–1403.
[5] G.W. Hohmann, Three dimensional EM modeling, Geophys. Surv. 6 (1983) 27–54.
[6] A.A. Kaufman, G.V. Keller, The magnetotelluric sounding methodMethods in Geochemistry and Geophysics, vol. 15, Elsevier Scientific Publishing Company, 1981.
[7] D.W. Marquardt, An algorithm for least squares estimation of nonlinear parameters, J. Soc. Industr. Appl. Math. 11 (1963) 431–441.
[8] R.L. Mackie, T.R. Madden, Three-dimensional magnetotelluric inversion using conjugate gradients, Geophys. J. Int. 115 (1993) 215–229.
[9] R.L. Mackie, T.R. Madden, P.E. Wannamaker, Three-dimensional magnetotelluric modeling using difference equations – theory and comparisons to integral equation solutions, Geophysics 58 (1993) 215–226.
[10] T. Mogi, Three-dimensional modeling of magnetotelluric data using finite element method, J. Appl. Geophys. 35 (1996) 185–189.
[11] P. Monk, Finite element methods for Maxwell's equationsNumerical Mathematics and Scientific Computation, Oxford University Press, New York, 2003.
[12] J.-C. Nédélec, Mixed finite elements in $\mathbf{R}^3$, Numer. Math. 35 (3) (1980) 315–341.
[13] G.A. Newman, D.L. Alumbaugh, Three-dimensional magnetotelluric inversion using non-linear conjugate gradients, Geophys. J. Int. 140 (2000) 410–424.
[14] R.G. Pratt, Seismic waveform inversion in the frequency domain, Part I: theory and verification in a physical scale model, Geophysics 64 (1999) 888–901.
[15] R.G. Pratt, C.S. Shin, G.J. Hicks, Gauss–Newton and full Newton methods in frequency-space seismic waveform inversion, Geophys. J. Int. 133 (1998) 341–362.
[16] W. Rodi, A technique for improving the accuracy of finite element solutions for magnetotelluric data, Geophys. J. Roy. Astr. Soc. 44 (1976) 483–506.
[17] W. Rodi, R.L. Mackie, Nonlinear conjugate gradient algorithm for 2-D magnetotelluric inversion, Geophysics 66 (1) (2001) 174–187.
[18] J.E. Santos, Global and domain-decomposed mixed methods for the solution of Maxwell's equations with application to magnetotellurics, Numer. Meth. Partial Differential Equations 14 (4) (1998) 407–437.
[19] D. Sheen, Approximation of electromagnetic fields: Part i. Continuous problems, SIAM J. Appl. Math. 57 (6) (1997) 1716–1736.
[20] C. Shin, K. Yoon, K.J. Marfurt, K. Park, D. Yang, H. Lim, S. Chung, S. Shin, Efficient calculation of a partial-derivative wavefield using reciprocity for seismic imaging and inversion, Geophysics 66 (2001) 1856–1863.
[21] C. Shin, S. Jang, D.J. Min, Improved amplitude preservation for prestack depth migration by inverse scattering theory, Geophys. Prosp. 49 (2001) 592–606.
[22] C. Shin, D. Min, Waveform inversion using a logarithm wavefield, Geophysics 71 (3) (2006) R31–R42.
[23] J.T. Smith, J.R. Booker, Rapid inversion of two- and three-dimensional magnetotelluric data, J. Geophys. Res. 96 (B3) (1991) 3905–3922.
[24] A. Tarantola, Inverse problem theory and methods for model parameter estimationSoc. Industr. Appl. Math. (SIAM), 2005.
[25] P.E. Wannamaker, J.A. Stodt, L. Rijo, Two-dimensional topographic responses in magnetotellurics modeled using finite elements, Geophys. J. Roy. Astr. Soc. 51 (11) (1986) 2131–2144.
[26] P.E. Wannamaker, J.A. Stodt, L. Rijo, A stable finite element solution for two-dimensional magnetotelluric modeling, Geophys. J. Roy. Astr. Soc. 88 (1987) 277–296.
[27] J.T. Weaver, Mathematical Methods for Geo-electromagnetic Induction, Wiley, 1994.
[28] K. Yamane, S. Takasugi, K.H. Lee, A new magnetotelluric inversion scheme using generalized RRI method, J. Appl. Geophys. 35 (1996) 209–213.
[29] J. Zhang, R.L. Mackie, T.R. Madden, 3-D resistivity forward modeling and inversion using conjugate gradients, Geophysics 60 (1995) 1313–1325.
[30] F.I. Zyserman, L. Guarracino, J.E. Santos, A hybridized mixed finite element domain decomposed method for two dimensional magnetotelluric modelling, Earth Planets Spaces 51 (1999) 297–306.